FACTORS INFLUENCING THE FLUID FLOW AND HEAT TRANSFER IN ELECTRON BEAM MELTING OF TI-6AL-4V

by

TAO MENG

B.Eng., Huazhong University of Science and Technology, Wuhan, China, 2005

A THESIS SUBMITTED IN PARTIAL FULFILLMENT OF THE REQUIREMENTS FOR THE DEGREE OF

Master of Applied Science

in

The Faculty of Graduate Studies

（Materials Engineering）

The University of British Columbia
(Vancouver）

November 2009

Abstract

Electron Beam Cold Hearth Remelting (EBCHR) and its associated casting process is an important consolidation technique for the treatment of virgin titanium sponge and scrap. The development of robust models to describe the casting process hinge on accurately capturing heat transfer phenomena within the ingot and fluid flow phenomena within the liquid pool. The flow field that develops within the liquid pool is influenced by several factors including buoyancy driven flow due to thermal gradients within the pool, surface tension, or Marangoni, driven flow due to the large thermal gradients induced on the surface by the Electron Beam and the ability of the mushy, or semi-solid, zone to attenuate the flow.

A mathematical model describing fluid flow and heat transfer in a Ti6Al4V button sample during electron beam melting has been developed to examine the relative contribution of the three factors cited above on the pool profile and flow field within the pool. The model has also been used to compare the steady state solution for a time averaged circular beam pattern with a transient solution obtained for the case where the beam pattern is comprised of a series of discrete points scribing the same circle. The latter, in which the beam spot is periodically stationary for small but finite periods, is intended to more closely mimic the industrial process.

The model is also used to examine the sensitivity of the predictions to changes in numerical and process parameters. The results indicate that the electron beam power and heat transfer coefficient have the largest influence on the liquid pool profile while the surface tension coefficient has little effect (i.e. 25% change in electron beam power results in ~25% liquid pool profile while 100% change in time step results in less than 1% in prediction).

Table of Contents

List of Tables

List of Figures

Acknowledgements

I would like to thank a lot of people who contributed to the production of this thesis. First of all, I would like to express my deep appreciation for Dr. Steve Cockcroft and Dr. Daan Maijer for their input and helpful advice on developing the mathematical model. I would also acknowledge the TIMET Corp. in Morgantown, Pennsylvania, USA, for their financial support and the experimental data.

I would like to thank Dr. J. Zhu for discussion on computational fluid dynamics. I would also thank for Dr. Denis Favez for his help on the thesis. Mr. Riley Shuster's help on using Ansys CFX 11.0 is appreciated.

Finally, I would like to express my gratefulness and thankfulness to my parents for their constant love and support from day one until now.

1. Introduction

1.1 Titanium Alloys and Their Applications

Titanium, discovered in 1791, is the ninth-most abundant element in the Earth's crust (0.63% by mass) [1] and the fourth-most prevalent metallic element (exceed only by Al, Fe, and Mg). Although discovered more than a century before, titanium was not purified until 1910 because the processes required to extract titanium from its various ores were laborious and costly [2]. As a metallic element, titanium is recognized for its high strength-to-weight ratio. It is a metal with low density (4500 kg/m^3) that is quite ductile (especially in an oxygen-free environment) [3]. Its relative high melting point (over 1,649 ºC or 3,000 ºF) makes it useful in high temperature applications. The most noted chemical property of titanium is its excellent resistance to corrosion due to the formation of a very adherent oxide film (it is almost as resistant to chemical corrosive attack as platinum) [4].

Titanium and its alloys were not commercially used until 1946 due to their high production cost. Despite its relatively high cost, the advantages offered by titanium alloys over other metals have led to their extensive use in a number of industrial applications including aerospace, chemical processing, automotive, sporting goods and architecture. Because it is biocompatible (non-toxic and not rejected by the body), titanium is also used in medical applications including surgical implements and implants [5].

1.2 Titanium Production and Fabrication

The production of titanium components occurs in four major stages [6]: i) reduction of titanium ore into "sponge"; ii) melting of the sponge, or sponge plus a master alloy to form an ingot; iii) primary fabrication, where it is cast to shape or ingot is converted into general mill

products such as billet, bar, plate, sheet, strip, and tube; and iv) secondary fabrication of finished shapes from mill products.

1.2.1 Reduction

Because titanium has a very high affinity for oxygen, it is difficult to produce titanium by direct reduction of its oxide at high temperature. The dominant commercial process for the production of titanium metal is the Kroll process.

The Kroll process is a complex and expensive batch process. In the Kroll process, the oxide is first converted to chloride through carbochlorination, whereby chlorine gas is passed over titanium mineral in the presence of carbon to make $TiCl_4$. $TiCl_4$ is then purified by fractional distillation and then reduced with 800ºC molten magnesium in an argon atmosphere to form pure titanium [3].

An alternative and more recent process that is undergoing evaluation for commercial application is the Fray-Farthing-Chen (FFC) Cambridge process. The process is an electrochemical method that works by direct reduction of solid TiO_2, in which the oxygen is ionized, dissolved in a molten salt and discharged at the anode, leaving pure titanium at the cathode [7].

This method uses titanium dioxide powder as feedstock to make the end product which is either a powder or sponge. The FFC Cambridge process effectively lowers the production cost by eliminating the conventional multi-step Kroll process. The FFC Cambridge process may render titanium a less expensive material for future industrial applications although there still exist significant technical challenges before commercialization can be realized.

1.2.2 Melting

After titanium ore is converted into sponge, it is necessary to consolidate it into a primary ingot through melting and casting operations prior to further downstream processing. Because titanium and its alloys are highly reactive at high temperature, special technologies are used to produce ingots of both pure titanium and the various titanium alloys. There are two main melting processes used in primary consolidation: vacuum arc remelting (VAR) and cold hearth melting (CHM); the latter using either plasma or electron beam as the heat source respectively [7].

1.2.2.1 Vacuum Arc Remelting

The Vacuum Arc Remelting (VAR) process is the most widely used melting process for consolidating titanium [7]. Prior to VAR processing, sponge is formed into compacts (usually 1/2 cylinder in a hydraulic press and then welded together). For many applications, the welding takes place in an inert gas (argon) chamber. This cylinder, referred to as an electrode, is then put into a large cylindrical water-cooled copper crucible of a slightly larger diameter, which is then closed and pumped down to attain a metallurgical vacuum environment. To begin the melting process, the electrode is first rested on the bottom and then raised until the arc initiates. The electrode is then progressively melted to form an ingot of the diameter of the crucible.

The use of this technology presents several advantages [8]:

1) Removal of dissolved gases, such as hydrogen and CO;
2) Reduction of undesired trace elements with high vapor pressure;
3) Achievement of directional solidification of the ingot from bottom to top, thus avoiding

macro-segregation and reducing micro-segregation.

However, producing high quality VAR ingots requires accurate control of the melt rate and the electrode gap. The retention of undesirable low- or high-density inclusions can also be a problem in the finished product [7].

1.2.2.2 Cold Hearth Remelting

There are two types of cold hearth remelting (CHR) processes: plasma-arc cold hearth remelting (PACHR) and electron beam cold hearth remelting (EBCHR). In the PACHR process, one or several plasma troches are used as heat sources to melt the feedstock, whereas in EBCHR process, one or more high powered electron beams are used in the process as heat sources instead of plasma torches [9]. The PACHR process is operated under an inert atmosphere and the EBCHR process is operated under a vacuum. Both processes contain the liquid titanium in a “skull” formed from the liquid metal as it freezes against water-cooled copper (liquid titanium is highly reactive and is nearly a universal solvent prohibiting the use of refractories for containment).

The schematics of the PACHR and EBCHR processes are shown in **Figure 1.1** and **1.2,** respectively. In general, there are three separate regions (melting, refining, and casting) in a typical CHR furnace [10]. Titanium sponge and scrap are first charged into the water cooled copper melting hearth (retort), located at one end, where they are melted by several moving plasma torches or electron beams. The molten metal then flows along a water-cooled copper refining hearth. In the refining hearth, the low density inclusions (LDI) dissolve in the liquid metal and/or evaporate through continuous heat input from the heat sources. The high density inclusions (HDI) sink to the bottom of the liquid pool and are then trapped in the skull. The

molten titanium then flows into the mold, where it is solidified and is withdrawn as a slab shaped or round shaped ingot. In certain furnace configurations, two refining hearths (see **Figure 1.1**) can be used in tandem to increase the efficiency of removing detrimental inclusions. The melting and refining regions can also be co-located on the same hearth (see **Figure 1.2**).

The CHR processes are different from the conventional VAR process in that the melting and casting steps are not inherently coupled and can be independently controlled. This attribute, and in particular the residence time of the liquid metal in the refining hearth, allows CHR to remove detrimental inclusions as well as the flexibility to use various forms of input materials, including sponge and machine turnings. This raw material flexibility makes the CHR processes able to produce ingot at a lower cost compared to VAR, which requires the use of virgin sponge, as well as allowing the production of a variety of titanium products [11, 12].

The EBCHR process is operated in a vacuum environment, which can, depending on the alloy, cause significant evaporation loss of high vapor pressure elements such Al and Cr resulting in challenges in controlling ingot chemistry. In contrast, because the PACHR is operated under an inert gas atmosphere (He or Ar), ingots produced using this process typically do not have a problem with chemistry control. However, PACHR ingots can have porosity due to the presence of He and/or Ar gas trapped in the solid [7]. Because there is no potential for gas entrainment in EBCHR process and because it offers superior LDI and HDI inclusion removal associated with the vacuum environment and the quiescent liquid conditions existing with the refining hearth, the EBCHR may be more suitable than PACHR

for low alloyed titanium metals (e.g. for Ti-6Al-4V).

Although successfully applied in production, certain technical difficulties associated with the PACHR and EBCHR processes need to be overcome. The primary difficulty for EBCHR, the subject of this research, is chemistry control.

1.2.2.3 VAR vs. EBCHR

The EBCHR process has several key advantages over the VAR process [13]: 1) the fact that melting is conducted in a higher vacuum environment and that the liquid metal is exposed to that environment a relatively long time enables more complete degassing and dissolution of low-density inclusions; 2) the long residence time of the molten titanium in the hearth and the relatively quiescent liquid pool allows any high-density inclusions contained with the scrap charged to the furnace to fall to the bottom of the melt and become trapped in the skull; 3) it allows handling of a wider range of feed stock (e.g. scrap); 4) non-axisymmetric shapes, such as slabs and bars can be cast; and 5) it offers considerable potential with regard to the control of metallurgical structure and surface quality because of the wide range of melting and casting conditions that are feasible.

Despite these advantages there are a number of challenges that remain for the EBCHR process [10]: 1)the EBCHR is conducted in a high vacuum, and the depth of the melt pool in the cold hearth is typically very shallow. This can lead to excessive reduction in the content of low melting-point, high vapor-pressure elements, such as aluminum and chromium from the molten titanium alloy. Thus, it can be a challenge to control the chemical composition of the final product ingot. 2) The liquid mixing inside the ingot of EBCHR is generally inferior to VAR process. The poor mixing results in a lack of chemical homogeneity in the final ingot produced

via EBCHR.

1.2.3 Primary and Secondary Fabrication

The conversion of ingot into general mill products – e.g. billet, bar, plate, sheet, strip, extrusions, tube, and wire – is defined as primary fabrication [6]. Forging, shape casting, powder metallurgy, and joining techniques used to produce a finished product are secondary fabrication. Mill products can readily be used in secondary manufacture of parts and structures.

Because the properties of titanium are so readily influenced by processing, great care must be taken in controlling the conditions under which the processing is carried out. At the same time, this characteristic of titanium makes it possible for the titanium industry to serve a wide range of applications with a minimum number of grades or alloys. By varying thermal or mechanical processing, or both, a broad range of special properties can be produced commercially for pure titanium and titanium alloys.

Primary fabrication is very important in establishing final properties because many secondary fabrication processes have little or no effect on metallurgical characteristics. Some secondary fabrications, such as forging and rolling do impart sufficient reduction to play a major role in establishing material properties.

1.3 Fluid Flow in EB Casting

The casting operation associated with the EBCHR process is batch or semi-continuous and therefore operates in three distinct phases: 1) start-up, 2) steady state and 3) final transient state. Referring to **Figure 1.2**, to begin, liquid metal is added to the container that is formed by placing the starter block or dovetail at the bottom of the water-cooled copper mould. Once the metal level reaches the desired height on the mould wall, the starter block is gradually

withdrawn downward forming the ingot. The rate of withdrawal is varied to keep the molten metal level at a prescribed height on the mould wall for a given metal flow rate. During the transient start-up phase the liquid pool profile, or sump, continues to evolve with time until it reaches a fixed depth dependent on the ingot cross section and metal feed rate. Steady state conditions then prevail until the ingot reaches the desired length, dictated by either the customer's requirements or equipment limitations. Liquid metal feeding is then suspended and the process enters the third stage, which is the second transient, during which the liquid sump depth decreases with time. Throughout the startup phase and steady state casting operation the top surface of the ingot is continuously heated with an electron beam to keep the top surface molten and maintain a good cast surface morphology. During the final transient the top may also be heated for a period of time with the electron beam to maintain the top surface molten and help avoid the formation of shrinkage voids deep within the steady state liquid sump. This process is called *hot topping* [13]).

A schematic illustration of the heat transport and fluid flow occurring within the casting operation associated with the EBCHR process is shown in **Figure 1.3**. As can be seen there are a number of inputs and outputs of heat that need to be described. Within the liquid pool, or sump, there are also complex fluid flow patterns that develop that strongly influence the heat transport and subsequently the pool profile, as well as the evaporation rates from the free liquid surface. This flow also affects the formation of casting defects associated with macro segregation, such as "beta fleck" in alpha-beta titanium alloys [6].

The fluid flow patterns in the liquid pool of the casting are the result of several factors. First, the continuous addition of feed material at the top of the ingot on one side induces fluid

flow. The fluid flow in the molten pool is also strongly influenced by the buoyancy (natural convection) and Marangoni (surface tension) forces. Buoyancy driven flow is induced in the liquid by density differences that may be caused by temperature gradients and/or concentration gradients. In electron beam melting there are temperature gradients within the melt induced by the input of heat at the top surface and the withdrawal of heat from the sides of the ingot to the mould and water-cooled containment vessel below the mould. As a result cooler fluid prevails adjacent to the mushy zone that drives fluid down the solid/liquid boundary toward the centre of the ingot and then upward in the centre leading to a convective cell or cells. This process advectively transfers heat within the liquid sump.

Since a liquid with a high surface tension pulls more strongly on the surrounding liquid than one with low surface tension, the presence of a gradient in surface tension will naturally cause the liquid to flow from regions of low surface tension to regions of high surface tension. The resulting flow is called Marangoni flow. The surface tension gradient can be caused by a temperature gradient or concentration gradient (surface tension is generally a function of both temperature and composition in metals).

Solidification results in a transformation from the liquid phase, in which an infinitesimal shear force causes permanent and continuous deformation, to a solid phase which may deform elastically or plastically. Usually the solid, mushy zone and liquid are treated as a single continuum with varying properties where a transformation from fluid to solid behavior is conducted by dampening the flow to the casting velocity. Darcy flow will often play this role and resist the flow in the mushy zone.

In the case of the EBCHR process, the intense heating at the top surface of the ingot leads

to large localized temperature gradients and, depending on the alloy, there may also exist gradients in concentration at the surface due to preferential depletion of volatile alloy constituents. Thus, both buoyancy and Marangoni forces potentially have an important role in the flow of fluid and transport of heat in the electron beam casting process of titanium alloys and therefore on development and evolution of the liquid sump profile. The current research is focused on the relative influence of these forces on the fluid flow and heat transfer during EB casting of Ti-6Al-4V. Mathematical modeling will be used to perform this analysis.

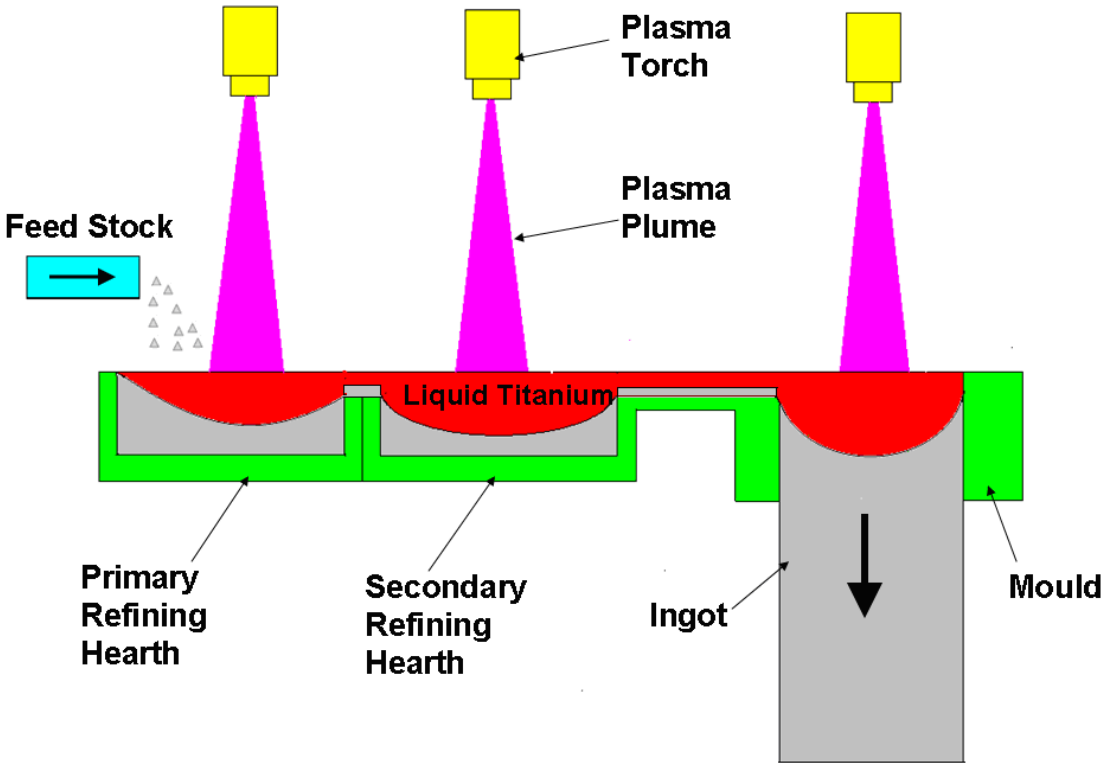

Figure 1.1 Schematic of plasma arc cold hearth remelting process

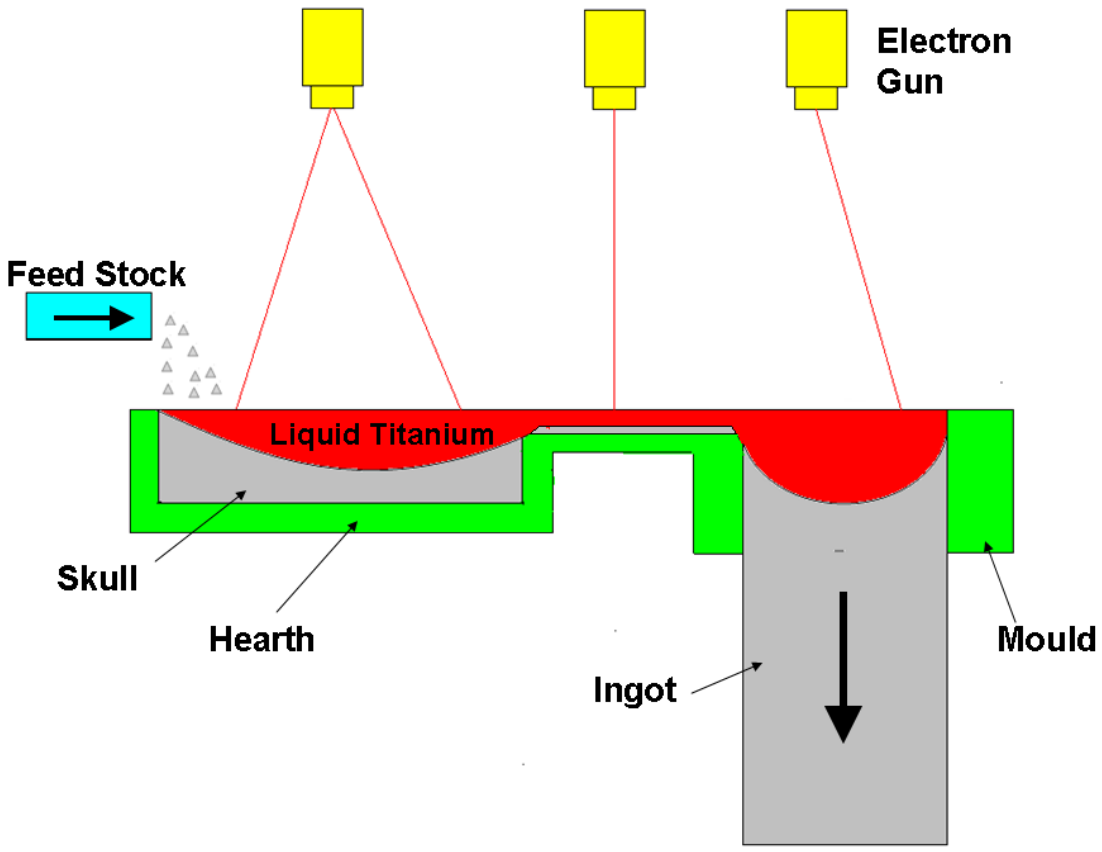

Figure 1.2 Schematic of electron beam cold hearth remelting process

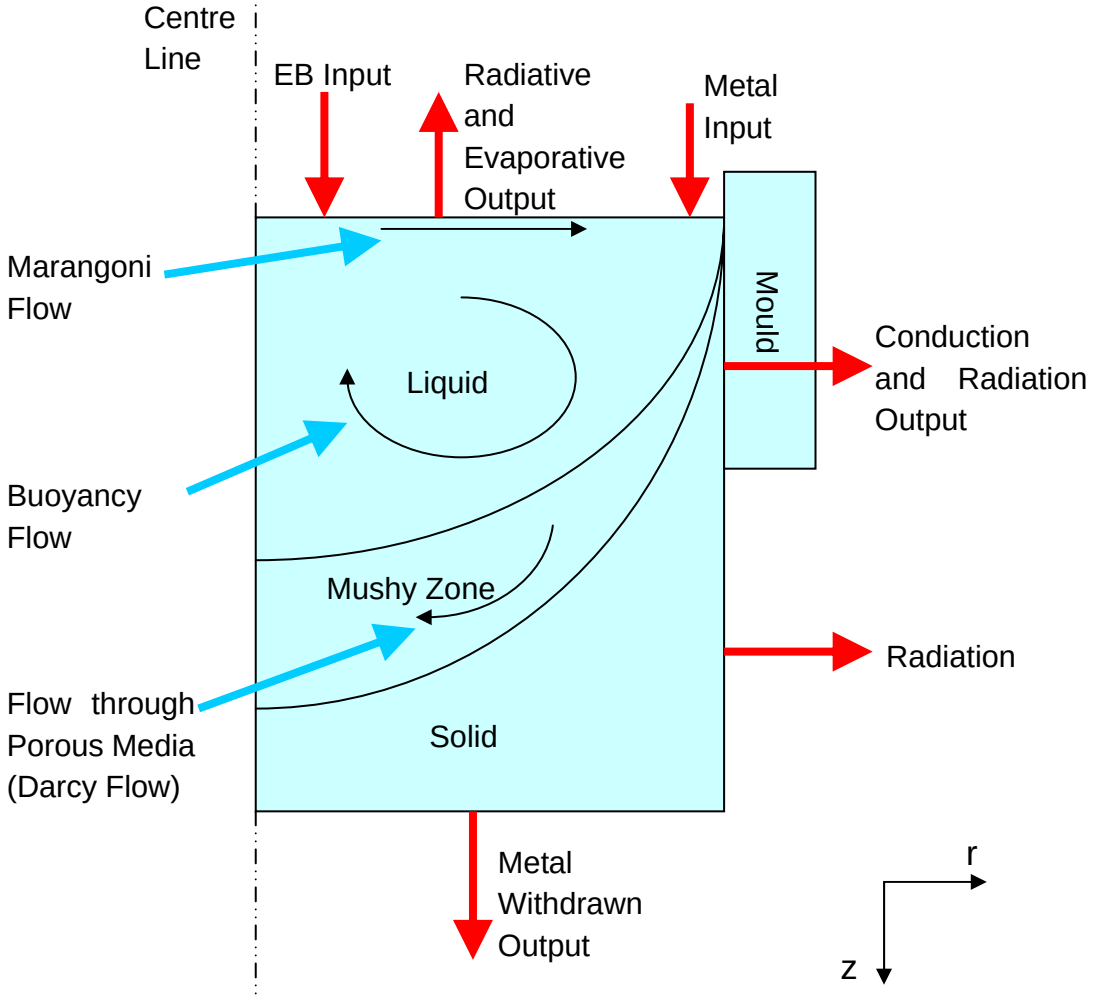

Figure 1.3 Schematic illustration of the electron beam casting process

2. Literature Review

The EB melting and remelting processes are usually complex and are characterized by a number of features which make in-situ measurements difficult [14]:

1) High temperature
2) The reactivity of the alloys

In this context, mathematical modeling based on physical-chemical phenomena offers a means of investigation provided that it is done in close association with laboratory measurements and experimental validations. Present day computer systems are sufficiently powerful to allow coupling of macroscopic and microscopic aspects for small domains.

A good mathematical model of EB melting should include the following phenomena:

1) A comprehensive heat balance, including heat input from the electron beam, heat losses from evaporation, radiation from various surfaces and conduction to the mould and heat generation from the latent heat associated with the solid/liquid transformation
2) Fluid flow, including buoyancy, Marangoni and Darcy flows

This literature review considers the published work in the areas of modeling of EB casting of superalloys, steel, aluminum, and titanium alloys. Before presenting the modeling of EB melting, the background theory on Marangoni flow is first introduced since Marangoni flow is a focus of the current research.

2.1 Marangoni Flow

In the case of liquid metal, surface tension is found to vary with temperature and composition [15]. Variations in temperature and composition on the surface of liquid metals

will therefore result in a net force on the liquid surface acting from areas of low surface tension to high surface tension. Mathematically the Marangoni force can be expressed in terms of the: 1) variation of surface tension with temperature $\partial\sigma/\partial T$ and 2) variation of surface tension with composition $\partial\sigma/\partial C$ as follows:

$$F_M(T,C) = \frac{\partial\sigma}{\partial T}\frac{\partial T}{\partial n} + \frac{\partial\sigma}{\partial C}\frac{\partial C}{\partial n} \tag{2.1}$$

where σ is the surface tension (N m^{-1}), T is the temperature (K), C is the concentration (kg m^{-3}), n is the direction normal. The terms $\partial\sigma/\partial T$ and $\partial\sigma/\partial C$ are referred to as the surface tension coefficients with respect to temperature (N m^{-1} K^{-1}) and concentration (N m^{-1} kg^{-1}), respectively.

A hypothetical Marangoni-induced flow pattern in an electron beam button melting process with a stationary beam located at the center of the top surface is shown schematically in **Figure 2.1.** Two potential flow patterns are presented associated with surface tension coefficients ($\partial\sigma/\partial T$) of differing sign. When the surface tension coefficient is negative (e.g. Ti-6Al-4V), the flow will be directed outward from the center, resulting in a wider and shallower liquid pool. However, when $\partial\sigma/\partial T$ is positive, the flow will be inward resulting in a narrower and deeper pool.

The Marangoni number (Ma) is an important dimensionless number related to Marangoni flow which is proportional to the thermal (Ma_T) or solutal (Ma_S) Marangoni forces divided by the viscous forces and a dissipation term. The Marangoni numbers can be expressed as [16,17]:

$$Ma_T = -\frac{\frac{\partial\sigma}{\partial T}\Delta TL}{\mu\alpha} \tag{2.2}$$

$$Ma_S = -\frac{\frac{\partial\sigma}{\partial C}\Delta CL}{\mu D} \tag{2.3}$$

where ΔT is the temperature difference between two characteristic points (K), L is the distance between them (m), μ is the dynamic viscosity (Pa s), $\alpha=k/\rho c_p$ is the thermal diffusivity of the liquid metal (m^2 s^{-1}) with ρ is the density of the liquid (kg m^{-3}), c_p is its heat capacity at constant pressure (J kg^{-1} K^{-1}) an dk is the thermal conductivity (W m^{-1} K^{-1}) , ΔC is the composition difference between two characteristic points, and D is the diffusivity of the surface active elements (m^2 s^{-1}). For EB melting of Ti-6Al-4V, depending on the power input and scan rate of the electron beam, intense localized surface heating may result in a large thermal and a large compositional gradient (due to localized Al evaporation), both of which could lead to the development of a significant Marangoni force, locally influencing the fluid flow and transport of heat.

2.2 Modeling of EB melting

A heat transfer-only model was used to simulate the steady state EB melting of copper, titanium, and aluminum by Vutova et al. [18]. A 2-dimensional axisymmetric formulation was used with heat transfer coefficient boundary conditions. The simulation results correctly show the expected trend when parameters such as the EB power, energy distribution, thermal and physical properties of the liquid and solid metal where altered. However, they failed to predict the liquid metal pool's depth and profile, as their model did not consider the effect of fluid flow. Nakamura et al. [19] attempted to include the effect of fluid flow by developing heat conduction models with enhanced thermal conductivity at the temperatures above the solidus to approximate the effect of advective transport of heat. However, because the fluid flow regimes within an EB melted liquid can be complex uniform enhancement of heat transport will not generally reflect that actual situation and it is necessary to develop fully coupled

thermal-fluid models [13, 20-24].

Fully coupled thermal-fluid models are based on the solution of the governing equations which describe the conservation of mass, momentum, and energy, as shown in **Equations (2.4)**, **(2.5)** and **(2.6)**, respectively, in three-dimensions [13, 21-24].

$$\frac{\partial \rho}{\partial t} + \nabla \cdot (\rho \mathbf{u}) = 0 \tag{2.4}$$

$$\frac{\partial \rho \mathbf{u}}{\partial t} + (\mathbf{u} \cdot \nabla)\rho \mathbf{u} = \mu \nabla^2 \mathbf{u} - \nabla P + \mathbf{S}_M \tag{2.5}$$

$$\frac{\partial \rho C_p T}{\partial t} + \rho C_p \mathbf{u} \cdot \nabla T = \nabla \cdot (\lambda \nabla T) \tag{2.6}$$

where t is the time [s], u is the velocity vector [m s^{-1}], x is the length [m], P is the static pressure [Pa], τ_{ij} is the stress tensor [Pa], S_M is a momentum source term [kg m^{-2} s^{-2}], H is the enthalpy [J kg^{-1}], and S_E is an energy source term [W m^{-3}]. For Newtonian fluids, such as molten metals [24], the stress tensor is linearly proportional to the rate of the deformation tensor γ, and viscosity μ [Pa s] as shown below.

$$\tau_{ij} = 2\mu \dot{\gamma} = \mu \left(\frac{\partial u_i}{\partial x_j} + \frac{\partial u_j}{\partial x_i} \right) \tag{2.7}$$

Techniques to describe the basic thermal-fluid conditions active during EB melting are discussed in the following section. Other phenomena relevant to casting problems, such as flow damping within the mushy zone, buoyancy, Marangoni and possibly, turbulence, depending on the flow behavior are also discussed.

2.2.1 Heat Transfer

2.2.1.1 Heat Input

The main heat input in EB melting and casting is from the electron beam. The electron beam is generally programmed to scan a pattern on the surface of the material being heated

[21]. The pattern may be comprised of geometric features such as circles, ellipses or lines. The geometric pattern is generated by a series of n points which represent the points on the surface where the beam dwells for a period of time before moving to the next point in the sequence. The dwell time is defined by a combination of the number of points in each geometric feature, the number of geometric features in each pattern and the time taken to complete the scan. The beam size, or spot footprint, used in industry is relatively small, resulting in a very high energy density where the beam dwells on the surface. Usually the heat flux distribution within the beam spot is assumed to be described by a Gaussian distribution as given below in **Equation (2.8)**.

$$q(r) = q_o e^{-\frac{r^2}{r_\sigma^2}} \tag{2.8}$$

where r is the distance from the beam center [m], r_σ is the standard deviation, and q_o is the total flux.

All of the relevant studies [13, 22, 23] approximate the energy input into the molten pool from the electron beam as a time-averaged heat flux. There are two reasons for this approximation:

1) The time required for the electron beam to trace the pattern in industrial applications is generally relatively short, on the order of 1s, thus large transients in surface temperature are avoided.
2) The computational time to fully describe the translation of the spot to generate the patterns/scan is prohibitive rendering most industrial problems intractable.

While this approach may be satisfactory in predicting the pool profile, it is unclear whether it is suitable for predicting evaporation as it will under predict peak surface temperatures

associated with the time the spot dwells on the surface. Likewise, the Marangoni driven flows associated with phenomena at the spot will also be under predicted.

In transient models where material is undergoing solidification or models involving the transport of material through a fixed domain – e.g. casting - the latent heat must be incorporated in the model by using either a source term [25, 26] or an effective specific heat [13, 23, 24]. The source term method requires the definition of the energy source term, S_E, in **Equation (2.6)** as:

$$S_E = \rho L \frac{\partial f_S}{\partial t} \tag{2.9}$$

where L is the latent heat released [J kg^{-1}], and f_s is the fraction solid. Alternatively, by calculating an effective specific heat, as shown in **Equation (2.10)**, the latent heat of solidification may be implicitly included in the enthalpy [27].

$$C_{P,eff} = C_P - \frac{df_S}{dT} L \tag{2.10}$$

Wei et al. [28] found that the computational time for the effective specific heat method is at least 20 times faster than for the source term methods.

2.2.1.2 Heat Output

Heat is transferred within the Electron beam casting process by convection within the liquid pool, conduction within the solid and via either radiation and/or contact conduction from the external or free surfaces dependent on the location of the surface. On the liquid free surface there is also heat loss associated with the evaporation of volatile species.

Radiation

As the electron beam casting process occurs within a vacuum, radiative heat transfer dominates from all of the free surfaces of the ingot, including the top and sides below the mould. The

Stefan-Boltzmann's law, also known as Stefan's law, has been used to model the radiation heat loss in EB melting by a number of researchers [13, 18, 19, 21-24]. Stefan's law states that a perfect radiator or blackbody will emit radiation from its surface at a rate q given by:

$$q = \sigma \varepsilon T^4 \tag{2.11}$$

where q is in W m^{-2}, and σ is the Stefan-Boltzmann constant (J s^{-1} m^{-2} K^{-4}). For the more general case of a grey body that emits a constant fraction of the black body radiation across all wave lengths, the left-hand-side of Eq. 2.11 is multiplied by, ε, the emissivity. In general for metals the radiation characteristics of the surface can be approximated by a wavelength dependent emissivity.

Conduction/radiation at an interface with a mould

The surface of the ingot adjacent to the water-cooled copper mould during continuous casting can be divided into three regions of heat transfer: the liquid-mould interface, the solid-mould interface and the gap region [24]. The meniscus region, in which surface tension causes localized curvature of the free surface adjacent to the mould wall, is generally ignored, as it is small. The heat flux from the three regions identified above is typically treated as a specified heat transfer coefficient boundary condition in which *h* may or may not be a function of time, location, and temperature [13, 18, 23, 24]. In most cases, expressing the heat transfer coefficient as a function of temperature is necessary as the transition from one region to the next is generally dependent on temperature. The typical heat transfer coefficient for liquid Ti-6Al-4V in contact with another metal is around 1500 W m^{-2} K^{-1} [13]. As cooling occurs, a solid skin forms between the liquid metal and the mould，causing the heat transfer coefficient to decrease. Continued cooling in casting process generally results in pull-away, the formation of a gap and a significant drop in magnitude of the heat transfer [13, 23, 24].

Evaporation

Isawa et al. [29] investigated aluminum evaporation from titanium alloys in an EB furnace, and proposed five sites from which aluminum could evaporate:

1) The feed stock,
2) Metal drops falling from the feed stock,
3) The hearth pool,
4) Metal drops from the hearth, and
5) The ingot.

The hearth pool was found to be the main evaporation site due to the large surface area exposed to the vacuum and relatively long residence times (1 – 10 min).

Aluminum losses during EBCHR processing of Ti-6Al-4V have been mathematically modeled in a number of studies using the Langmuir equation [30-32], which assumes interface-reaction-controlled kinetics and that the collision of atoms in the ambient atmosphere can be neglected. The general form of the Langmuir equation for the case of evaporation of species *i* in a multi component alloy is:

$$\dot{m} = \frac{\gamma_i M_i P_i^0 X_i}{\sqrt{2\pi M_i R_g T}} \tag{2.12}$$

where $\dot{m}$ is the flux density of ith element through evaporative surface [kg m^{-2} s^{-1}], P_i^0 is the vapor pressure of pure i^{th} element at the absolute temperature T [Pa]; γ_i, M_i and X_i are the activity coefficient, molar mass [kg mol^{-1}], and mole fraction, respectively, of element *i*; R is the gas constant [J mol^{-1} K^{-1}]; and T is the temperature of the evaporating metal [K]. Fukumo et al. [33] and Richie et al. [34] experimentally confirmed that the evaporative losses of aluminum can be estimated by the Langmuir equation. Akhonin et al. [35] developed a

diffusion model to predict the aluminum evaporation during EBCHR processes of titanium alloys. The Langmuir equation was implemented into their model as a boundary condition.

Heat loss by evaporation is the product of the Langmuir evaporation rate $\dot{m}$ and the latent heat of evaporation L_e as shown in **Equation (2.13)**.

$$q_{evap} = L_e \dot{m} \tag{2.13}$$

For typical aluminum evaporation during the electron beam melting of Ti-6Al-4V, the latent heat of evaporation L_e is around 10^7 J kg^{-1} [19].

2.2.2 Fluid Flow

As discussed, there are three important phenomena influencing the fluid flow field in the EB melting process: buoyancy, Marangoni forces and flow damping within the mushy zone. These factors should be included in coupled thermal-fluid models of EB melting. Turbulence during EB melting has also drawn the attention of a number of researchers.

Buoyancy

As discussed in the first chapter, buoyancy-induced flow occurs due to density variations, which cause denser liquid to sink and less dense liquid to rise. During EB melting, significant temperature gradients are present which produce large density gradients and depending on the alloy there can also be compositionally induced density gradients due to evaporation or segregation within the mushy zone. Two approaches have been used to treat the buoyancy-induced flow: applying a Boussinesq momentum source term [22], or using a 'full' buoyancy model [13, 23]. The Boussinesq approach approximates buoyancy flow as a momentum source, S_M, on the right side of momentum conservation **Equation (2.5)**.

$$S_{M,Buoyancy} = \rho_{ref} g \beta \left(T - T_{ref} \right) \tag{2.14}$$

where β is the volume thermal expansion coefficient [K^{-1}]. The Boussinesq approximation

accounts for the density variation only in the buoyancy term and the volumetric expansion coefficient β is assumed to be independent of temperature i.e. ρ varies linearly with T.

The 'full' buoyancy model uses the product of gravitational acceleration and the difference between a reference density and the current local density as a momentum source, S_M, on the right side of **Eq. (2.5)** and can be expressed as [38]:

$$S_{M,Buoyancy} = g(\rho - \rho_{ref}) \tag{2.15}$$

When using the 'full' buoyancy model, the density variation with temperature must be carefully selected to ensure the mass conservation. If the modeling domain is fixed, the density of solid should be constant.

Marangoni

Because of its effect on computational time, Marangoni driven flow has generally been neglected when modeling EB melting and casting [13, 23]. However, several researchers [21, 22, 39, 40] have included Marangoni flow in models of EB melting to provide a better understanding of the flow field. Generally, two methods have been used to incorporate Marangoni flow into these models: i) defining a surface tension boundary condition and ii) applying a Marangoni momentum source term.

The first method was developed assuming that the rate of change in surface tension must be balanced by the shear stress and resulted in the following formulation [39-41]:

$$\tau = -\mu\left(\frac{\partial u_z}{\partial x_z}\right) = \left(\frac{\partial \sigma}{\partial T}\right)\nabla T_{ij} \tag{2.16}$$

Equation (2.16) is issued as a surface boundary equation.

Marangoni flow can also incorporated through a momentum source term in **Equation 2.5** as [36]:

$$S_{M,Marangoni} = \left(\frac{\partial \sigma}{\partial T}\right) \nabla T_{ij} \tag{2.17}$$

The above two methods only consider the Marangoni effect caused by temperature variation. In addition to this effect, the composition changes of several active elements such as Si and O have been found to change the sign of the surface tension coefficient ($\partial\sigma/\partial T$) in materials such as superalloys and steels [36, 40]. Lee et al. [36] and Yang et al. [40] discussed the effects of Si and O compositional changes on fluid field, respectively. They used specific values of surface tension coefficients for **Equation (2.16)** according to the compositions in their EB melting models. For EB melting of IN718 with low-S content (6 ppm), Lee et al. [36] found that the surface flow was predicted to be outward from the center of the beam with a peak velocity of 0.16 m/s. With high-S content (20 ppm), the flow was observed to point inwards from the edge of the pool with a peak velocity of 0.19 m/s. Yang [40] observed that for the GTA welding of 304 stainless steel when the oxygen content increased, the convection pattern in the weld pool changed from predominantly outward convection (when oxygen content was <280 ppm), to outward at pool center together with inward on pool periphery (when oxygen content was in the range of 280-500 ppm), and finally to predominantly inward convection (when oxygen content was >500 ppm). These flow direction inversions are related to a change of the sign of the surface tension coefficient with the concentration of surface tension active elements.

Flow Damping within the Mushy Zone

Solidification results in a transformation form the liquid phase, in which shear forces are proportional to the rate of shear, normal forces cannot be supported and no strain is accumulated, to the solid phase, in which the full range of forces (3 normal and 3 shear) may

be present leading to the accumulation of elastic and potentially also plastic strains. Often the solid, mushy zone and liquid are treated as a single continuum with varying properties in a CFD model. In models of continuous casting processes in which an Eulerian frame of reference is adopted, the liquid motion transits to solid through the domain by dampening the flow to the casting velocity. Various methods have been used to take account for this damping: applying a Darcy-based momentum source term [21, 22, 25, 42], ramping viscosity [43] or a combination of two [13].

The most commonly used method to account for the flow damping within the mushy zone is with a Darcy-based momentum source term, as shown below:

$$S_{M,Darcy} = -\frac{\mu}{K}\left(u - u_{spe}\right) \tag{2.18}$$

where K is the permeability [m^2], and u_{spe} is a specific velocity (i.e. casting velocity) [$m\ s^{-1}$]. The permeability shown in **Equation (2.18)** is calculated using the Carman-Kozeny equation [45],

$$K = \frac{(1 - f_s)^3}{D f_s^2} \tag{2.19}$$

where D is a coefficient related to the solid/liquid interfacial area in the mushy zone and the volume of the geometry. Rappaz et al [44] has shown that the flow is significantly damped when the values of permeability are less than 10^{-8}-10^{-9} m^2.

Laminar and Turbulent Flow

Turbulence is a state of fluid motion, which is characterized by apparently random and chaotic three-dimensional vorticity. When turbulence is present, it usually dominates all other flow phenomena and results in increased energy dissipation, mixing, heat transfer, and drag. For casting models, it is important to prevent enhanced dissipative effects within the solid

associated with the inclusion of turbulence in solution algorithm. Shyy et al. [25] developed a method to eliminate enhanced heat transfer within the mushy zone and solid regions. This method was based on changing k-ε two-equation formation of eddy viscosity (**Equation (2.20)**), by using **Equation (2.21)** to calculate the C_μ coefficient rather than employing the traditional constant value of 0.09. By modifying the C_μ coefficient, the eddy viscosity is ramped down within the solid regions, which effectively eliminates turbulence in the solid and ensuring correct heat conduction.

$$\mu = \frac{C_\mu \rho k^2}{\varepsilon} \tag{2.20}$$

$$C_\mu = 0.09\left\{\sqrt{(1-f_S)}\cdot\exp\left[-\frac{3.4}{\left(1+\frac{\rho k_{tke}^2}{50\mu\varepsilon}\right)^2}\right]\right\} \tag{2.21}$$

where k_{tke} is the turbulent kinetic energy [m^2 s^{-2}], and ε is the turbulent eddy diffusivity [m^2 s^{-3}].

However, in the case of EB melting, as the casting speed is relatively small, laminar flow is used instead to simplify the model [13, 22, 23]. Bellot et al. [21] showed that the flow is weakly turbulent for a casting rate of 400 kg/hr during EB melting of Ti-6Al-4V round ingots.

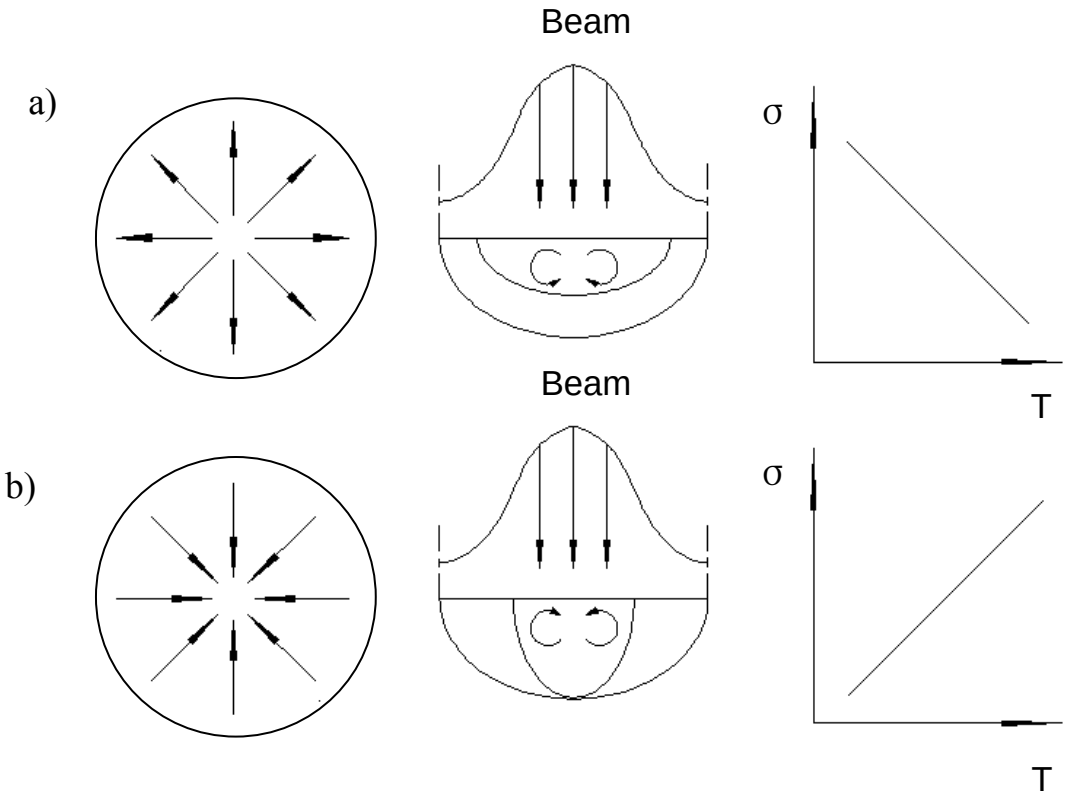

Figure 2.1 Hypothetical Marangoni-induced flow pattern in electron beam melting with a) negative and b) positive $\partial\sigma/\partial T$

3. Scope and Objectives

3.1 Objective of the Research Program

The purpose of the current research program is to determine the relative contributions of surface tension, buoyancy and mushy zone resistance on the thermal and fluid flow fields that develop during the Electron Beam casting of Ti-6Al-4V. Further, once these phenomena have been incorporated, to study the influence of different methods for describing the electron beam boundary condition – e.g. time averaged vs. fully transient – on the sump profile, surface temperature profile and near surface fluid flow. These objectives form part of an on-going research program to develop a comprehensive coupled thermal-fluid model of Ti-6Al-4V ingot casting associated with TIMET's EBCHR operation in Morgantown Pennsylvania.

3.2 Scope of the Research Program

A mathematical model of the electron beam button melting process is used as the basis for this investigation as the domain is relatively small yielding comparatively short solution times. The mathematical model described in the current program has been developed in the commercial Computational Fluid Dynamics (CFD) software package ANSYS-CFX 11.0.The model accounts for the power input to the top surface of a hemispherical button via an electron beam, radiation heat losses from the top surface and radiation and conduction through the sides/bottom in contact with the water-cooled copper mould.

The Marangoni force term has been incorporated into the model as a momentum source confined to the top surface. The buoyancy force term has also been included to account for the effects of temperature-dependent density. The Darcy force term has been implemented

into the model to attenuate flow in the mushy zone. The latent heat of solidification and the β/α transition have also been included in the analysis.

In order to validate the basic heat balance formulation, the model was first applied to simulate an experiment reported by Ritchie [23] on EB button melting of SS316, in which he measured the liquid pool profile and top surface temperature profile under two different power input conditions. Once validated against Ritchie's measurements, the model was applied to EB melting of a Ti-6Al-4V button to study the influences of Marangoni driven flow, buoyancy and flow damping both separately and in combination within the mushy zone on heat transfer and fluid flow. The efficacy of using a time-averaged heat flux boundary condition to represent the power input from an Electron Beam scanning a circular pattern on the button compared with the full transient solution in which the beam spot is sequentially moved then held at a series of spots on the surface to reproduce the pattern was also assessed with the model. Finally, a sensitivity analysis was conducted on the influence of numerical and process parameters on the predicted results.

4. Mathematical Model Development

Electron beam (EB) melting is a complex process involving many different transport phenomena as discussed in the literature review. The extent to which each of these phenomena is included in a mathematical model depends on the goal of the model. In this chapter, the details of a mathematical model developed to predict the temperature and velocity distribution during EB melting of Ti-6Al-4V will be presented. The model has been applied to a button melting case, but has been implemented in a manner that allows straightforward application to other configurations.

During EB button melting, the heat applied to the top surface by an electron beam melts a portion of the button depending on the motion of the beam. The area directly adjacent to the water-cooled copper mould remains solid. The majority of the heat loss from the button occurs from the top surface through radiation. Heat is also lost from the solid shell to the water-cooled copper mould. Within the button, heat transport occurs through the combined effects of advection (in the liquid) and diffusion.

As discussed in the literature review, there are three phenomena that influence fluid flow during EB melting which must be considered by the model: 1) Marangoni forces caused by surface tension variation due to large temperature gradients, 2) buoyancy forces generated by density variation, and 3) Darcy forces, or mushy zone resistance, which resists the flow in the mushy zone.

4.1 Model Assumptions

In developing the model described in this chapter, the following assumptions have been made:

1) The fluid flow in the liquid pool is laminar and incompressible.

2) The surface tension variation resulting from the concentration differences can be ignored.

3) The molten pool surface is flat.

4) The density in the solid and the surface tension coefficient are independent of temperature.

5) The heat flux distribution within the electron beam spot may be described by a Gaussian distribution.

4.2 Governing Equations

The conservation equations for mass, momentum and energy must be solved to predict the temperature and fluid flow fields during EB button melting. These equations are:

$$\frac{\partial \rho}{\partial t} + \nabla \cdot (\rho u) = 0 \tag{4.1}$$

$$\frac{\partial \rho u}{\partial t} + (u \cdot \nabla)\rho u = \mu \nabla^2 u - \nabla P + \rho_{ref} g + S_F \tag{4.2}$$

$$\frac{\partial \rho C_P T}{\partial t} + \rho C_p u \cdot \nabla T = \nabla \cdot (k \nabla T) \tag{4.3}$$

where g is the gravitational acceleration [m s^{-2}]. In the momentum equation, S_F is the sum of momentum source terms (Marangoni, buoyancy and flow damping within the mushy zone) acting on the liquid metal.

Momentum Source Term

In the model, the variation in density of liquid Ti-6Al-4V with temperature is accounted for and therefore temperature gradients within the liquid will result in a driving force for liquid flow – e.g. buoyancy driven flows. The momentum source term to describe the buoyancy effect is [38]:

$$S_{buoyancy} = (\rho - \rho_{ref})g \tag{4.4}$$

where ρ_{ref} is the density of the solid Ti-6Al-4V.

The surface tension or Marangoni driven flow has been introduced in the momentum source term as:

$$S_{Marangoni} = \frac{\partial \sigma}{\partial T}\frac{\partial T}{\partial n} \quad for \;\; z = 0 \tag{4.5}$$

The expression assumes a dependence only on temperature and no influence of compositional gradients – e.g. that the surface tension for Ti-6Al-4V is dependent on temperature and independent of composition. The calculation of this force is limited to surface regions of the casting where high thermal gradients are expected (i.e. the top surface heated by the electron beam).

A force to dampen flow in the mushy zone has been included in the momentum source term using Darcy's law:

$$S_{Darcy} = -\frac{\mu}{K}u \tag{4.6}$$

where μ/K is the Darcy momentum source term coefficient [kg m^{-3} s^{-1}]. In the current research, the mushy zone is treated as a porous medium, which allows the permeability to be calculated using the Carman-Kozeny equation [43]:

$$K = \frac{(1 - f_s)^3}{D f_s^2} \tag{4.7}$$

where D is a coefficient related to the solid/liquid interfacial area in the mushy zone and the volume of the geometry.

The overall momentum source term in **Equation (4.2)** is calculated by summing the component terms for the Buoyancy, Marangoni and Darcy forces as:

$$S_F = S_{buoyancy} + S_{Marangoni} + S_{Darcy} \tag{4.8}$$

Implementation of Latent Heat

For Ti-6Al-4V, latent heat is evolved during the liquid to solid and the β to α phase transformations. The effective specific heat method was chosen in the current modeling technique to include this heat source. In this method, the effective specific heat is increased to reflect the latent heat during the two transformations [27]:

$$C_{p,eff} = C_p + C_{p,latent} \tag{4.9}$$

where $C_{p,\ latent}$ is evaluated by the following equation:

$$C_{p,latent} = -L\frac{df}{dT} \tag{4.10}$$

During solidification, L corresponds to the latent heat released, and f is the fraction solid. The same equations are adopted for the β to α phase transformation, where L is the heat released during the β/α transformation and f is the fraction of α phase.

4.3 Geometry

There were three model domains employed in this work. The first model geometry employed was that of a rectangular domain which was used to validate the basic formulation and implementation of the Marangoni force subroutine within CFX. The geometry and the mesh are shown in **Figure 4.1**.

The second geometry employed is shown in **Figure 4.2** and was employed to reproduce the results from EB button melting experiment conducted by Ritchie on SS316 [23]. The comparison between the model predictions obtained using this model and experimentally derived pool profile and top temperature distribution were used to validate the formulation of the model for general application to EB button melting.

Having validated the basic model formulation, a model was developed and used for the main body of work to examine the influence of buoyancy, Marangoni, mushy zone dampening and beam pattern on the thermal and flow fields during EB button melting of

Ti-6Al-4V. The button model consisted of an inverted hemispherical cap with a radius of 50 mm and a depth of 25mm. The size was selected to be large enough to examine the basic phenomena of interest but small enough to allow multiple runs to be completed in a reasonable timeframe. The geometry and mesh of the calculation domain are shown in **Figure 4.3**. The geometry was meshed with ~20,000 tetrahedral elements which have a minimum element side length of ~1mm.

As the main body of the work was conducted using the EB button model for Ti-6Al-4V, the following sections detail the development of that model. Where appropriate the material properties and boundary conditions used in the other two models are described.

4.4 Materials Properties

Most of the material properties for Ti-6Al-4V used in the model were based on Mills [21]. In those instances where a different source was used the source has been cited. The temperature invariant properties are summarized in **Table 4.1** and the temperature variant properties are plotted in **Figure 4.4**, **4.5** and **4.6**. The solidus and liquidus temperatures of Ti-6Al-4V were selected as 1595 °C and 1625 °C, respectively based on Shyy [25]. The change to these temperatures from those reported by Mills [37] was required to obtain results that were in line with industrial practice [45].

The latent heat of solidification and the β/α phase transformation are 286,000 J/kg and 48,000 J/kg, respectively [37]. The modifications to the specific heat, $C_{p,\ latent}$, as a function of temperature were applied to account for latent heat evolution, as defined in **Equation (4.10),** for the liquid-to-solid and α-to-β transformations are shown in **Figure 4.5** and **Figure** 4.**6,** respectively.

The viscosity of liquid Ti-6Al-4V is 0.003 Pa • s [22]. During the liquid to solid transition, the viscosity in the mushy zone is exponentially increased to 3000 Pa • s to account for the flowing resistance within the mushy zone. In the current research, *D,* needed in Eq.4.7*,* has been set equal to 10^{10} m^{-2} based on simulation results [41].

4.5 Boundary Conditions

4.5.1 Thermal

The boundary conditions applied to the EB button melting model for Ti-6Al-4V are shown schematically in **Figure 4.7**. Boundary conditions are applied to two distinct surfaces on the button: i) the top surface, where heating from the electron beam and radiation heat losses occur, and ii) the surface that forms the interface with the water-cooled copper mould. The parameters for thermal boundary conditions are summarized in **Table 4.2**.

Top Surface

On the top surface of the button, heat is supplied by the electron beam and lost via radiation. Additional heat loss due to evaporation has been neglected due to the lack of experimental data necessary to quantify the rate of evaporation of Ti-6Al-4V.

The heat flux distribution around the beam at a stationary point is assumed to be a Gaussian distribution:

$$q_{EB} = AP_w e^{-\frac{r^2}{2r_\sigma^2}} \tag{4.11}$$

where r is the distance from the beam center, r_σ is the standard deviation of the beam, P_w is the total beam power (assuming no loss), and A is a constant dependent on the standard deviation. A has been calculated numerically by assuming a standard deviation and integrating the Gaussian function in r and θ via **Equations (4.12)–(4.15)**:

$$r_i = i \bullet 0.001 \tag{4.12}$$

$$S_i = \pi \left(\frac{r_i + r_{i+1}}{2} \right)^2 \text{ for } \qquad i = 0 \tag{4.13}$$

$$S_i = \pi \left(\left(\frac{r_i + r_{i+1}}{2} \right)^2 - \left(\frac{r_{i-1} + r_i}{2} \right)^2 \right) \text{for} \qquad i = 1, 2... \tag{4.14}$$

$$\sum_{i=0}^{\infty} A S_i e^{-\frac{r_i^2}{2r_\sigma^2}} = 1 \tag{4.15}$$

where i is an increment, r_i is the radius from the beam center at each increment, and S_i is the incremental area.

In the industrial EBCHR process, the electron beam moves across the surface being heated tracing a pattern formed by repeating shapes such as ellipse, circles, or straight lines, as previously described. Three different EB power input conditions were studied in this investigation: 1) centered, 2) moving EB, and 3) time-averaged EB. In the first case, the EB spot is stationary and positioned at the center of the top surface of the button. In the second case, the EB spot traces a circular pattern centered on the button centre with a radius of ½ the radius of the button. To be consistent with industrial practice, the circular pattern is generated by subdividing the pattern into a series of 256 points, each representing a point on the circumference of the circle where the beam spot dwells for a time equal to $\frac{1}{F \cdot 256}$ s, before moving on to the next spot in the sequence along the circle circumference. F is the pattern repetition frequency and frequencies of 0.1, 0.675, 1, 5 and 10 Hz where investigated. In the third case, a constant heat flux distribution is applied based on the time-averaged heat flux calculated from the moving EB case:

$$q_{EB} = \frac{t_i}{t} A P_w e^{-\frac{r^2}{2r_\sigma^2}} \tag{4.16}$$

where t_i is the dwell time of ith beam spot, and t is the total time required to draw the pattern. The resulting heat fluxes for these three cases are shown in **Figure 4.8**.

The radiation heat loss from the top surface to the furnace enclosure is described as follows:

$$q_{rd} = \sigma\varepsilon_{top}(T_S^4 - T_{chamber}^4) \tag{4.17}$$

where T_s is the temperature for top surface, and $T_{chamber}$ is the temperature of the furnace enclosure.

Since in the current EB button melting model heat loss by evaporation is not included, the total heat flux on the top surface of the button is given by **Equation (4.18)**:

$$q_{top} = q_{EB} + q_{rd} \quad for\ z = 0 \tag{4.18}$$

Bottom / Side Surface

The bottom / side surface which is in contact with the water-cooled copper mould loses heat through conduction and radiation. The heat flux on this surface is calculated by the following equation:

$$q_{side} = h_c(T_s - T_{mold}) \tag{4.19}$$

where h_c is a temperature dependent heat transfer coefficient, T_s is the temperature of the button surface, and T_{mold} is the temperature of the mould.

The heat transfer coefficient, shown in **Figure 4.9,** was similar to that used by Zhao [10]. The function consists of three regimes of behaviors: i) the high temperature range ($T>T_{liquidus}$) where the liquid metal is in direct contact with the mould resulting in constant contact resistance ($1/h_c$), ii) the transition temperature range ($T_{solidus}<T<T_{liquidus}$) where the contact heat transfer decreases linearly with temperature as the button surface transitions to being fully solid and surface irregularities result in a gradual separation of the surface from the mould, and iii) the low temperature range($T<T_{solidus}$) where heat transfer by radiation dominants, and h_c is calculated as $\sigma\varepsilon(T_s^2+T_{mold}^2)(T_s+T_{mold})$.

4.5.2 Flow Field

Fluid flow (velocity) boundary conditions are defined for the top and bottom / side surfaces of the button. On the top surface, a free slip condition is applied where only the velocity in the direction normal to the surface (z direction) is constrained to be zero. On the bottom / side surface, a no-slip condition is applied where the velocity is specified as zero in the directions normal and tangential to the surface.

4.6 Initial Conditions

In the EB button melting model, uniform initial conditions have been applied to the entire domain where the temperature is set to 1700 ºC, the velocity is set to 0 m/s and the pressure is set to 0 Pa.

4.7 Numerical Solution

The conservation equations described in section 4.1 have been solved for the Ti-6Al-4V button model subject to the boundary and initial conditions defined in sections 4.5 and 4.6. The commercial computational fluid dynamics software, ANSYS – CFX 11.0, was used to perform these calculations. CFX uses a control volume approach to solve the governing equations [22]. User subroutines were developed to apply the spatially varying heat flux of the electron beam and the surface tension driven force (the procedure used to develop and verify the surface tension flow subroutine is described below). The partial differential equations were integrated over all control volumes in the domain. This is equivalent to applying a basic conservation law (for mass, momentum and energy) to each control volume. These integral equations are converted into a system of algebraic equations by generating a set of approximations for the terms in the integral equations. Then the algebraic equations are

solved iteratively. All conservation equations and all variable components are stored at the center of the control volume.

The model was run in a transient mode. Each time the model was run, the EB button melting process was simulated for a sufficient time to reach steady state. Initially, a large time increment was used to reach near equilibrium conditions. The time step was then progressively decreased until the solution (temperature and velocity distributions) stopped changing and steady state was achieved. In the case of a simulation considering the moving EB spot, a cyclic steady state was achieved where the variation of the solution for each cycle was repeatable.

4.8 Model Validation

The implementation of the Marangoni force source term and the overall validity of the model were systematically tested during development. The results of two the test models used for this purpose are reported in this section.

4.8.1 Marangoni Force

A user subroutine was written in FORTRAN to apply the Marangoni force to every element on the top surface of the button. A simple test case was devised to assess the proper implementation of the subroutine and the accuracy of applying a force in this manner. A uniform temperature gradient in the x-direction was applied to a rectangular geometry and the resulting fluid velocity distribution was assessed. Water was chosen as the fluid because its properties, presented in **Table 4.3**, are well known. The geometry of the domain and mesh used as well as the constant linear temperature distribution applied to the domain are shown in **Figure 4.1**. The problem as defined would result in a Marangoni force proportional to the

temperature gradient applied along the upper surface of the domain. Two methods for applying the Marangoni force were investigated: i) calculated via the subroutine and ii) force calculated manually by **Equation (4.5)** and then applied directly in CFX without the subroutine. A no-slip condition was applied on the left and right faces of the domain. A free slip condition was applied on the top and bottom faces. The velocity within the domain was set to 0 m s^{-1} initially. The model was run for 1000s using a time step of 1s to reach a steady state.

The velocity vector plots of the results for the two methods of applying the Marangoni force are shown in **Figure 4.10**. In both cases, the water flows from the highest temperature region (left side) to the lowest temperature region (right side) on the top surface due to the Marangoni force. The fluid is then pushed down the right side of the domain, flows along the bottom surface before rising up the left side, to produce a recirculating flow. The direction and magnitude of the predicted velocities are identical for the two methods of applying the Marangoni force. Thus, the user subroutine to apply Marangoni force has been properly incorporated into the CFX.

4.8.2 Validation of the Coupled Thermal-Flow Model

Prior to employing the model to study the electron beam button melting process for Ti-6Al-4V, the formulation of the model in terms of the basic boundary conditions, implementation of the momentum source terms described above and the assumptions related the thermal-fluid materials properties must be validated. Ideally, this validation would be performed with data from a Ti-6Al-4V button, but this was unavailable. Instead, an investigation by Richie [23] on the electron beam button melting of SS316 was used. Richie

measured the surface temperature distribution during melting and the resulting pool profile. With few exceptions, the boundary conditions and material properties reported by Ritchie were applied directly to the current model.

A model based on a thin three-dimensional slice of the button geometry used by Richie was developed to compare with his experimental data (*Note: CFX does not have available a 2-D axi-symmetric formulation and hence a 3-D slice is needed to analyze the axi-symmetric button problem.*) The model domain and the boundary conditions are shown schematically in **Figure 4.2.** The geometry of the button was approximated by a rectangular domain with a mesh composed of 60 × 60 control volumes (1 element thick) as shown in **Figure 4.11**. The material properties for SS316 used in the model, reported by Richie [23], are summarized in **Table 4.4** and **Figure 4.12**. The processing conditions for the SS316 button melting experiments shown in **Table 4.5**.

The boundary conditions for the simulations are shown schematically in **Figure 4.2**. The left side boundary is the centerline. Employing the methodology described in Section 4.5, heat flux boundary conditions for electron beam heating and heat loss due to radiation were applied to the top surface of the button. A stationary electron beam with two different focus conditions was applied to the center of the button in these experiments. Thus, two different heat flux distributions were applied in the model: i) a diffuse beam (standard deviation of 0.025m) and ii) a focused beam (standard deviation of 0.003 m). The heat flux distributions for these two cases are shown in **Figure 4.13**. In addition to the EB heating and radiation heat loss, heat loss by evaporation was also considered in this model because there was considerable mass loss observed during the experiments. The evaporative heat flux from the

top surface was calculated as the product of the Langmuir evaporation rate, $\dot{m}$, and the latent heat of evaporation, L_e (see **Table 4.4**):

$$Q_{evap} = L_e \dot{m} \tag{4.20}$$

$$\dot{m} = \frac{\gamma_i M_i P_i^0 X_i}{\sqrt{2\pi M_i R_g T}} \tag{4.21}$$

The mass fractions and activity coefficients of the alloying elements in SS316 are shown in **Table 4.6**. **Equation (4.22)**, a form of the Clausius-Clapeyron equation, was used with the empirical coefficients in **Table 4.7** to calculate the saturated vapor pressures of each element in its pure state:

$$P_i^0 = 133.3 \bullet 10^{\left(\frac{-A}{T} - B \bullet Log(T) - \frac{C \bullet T}{1000} + D\right)} \tag{4.22}$$

Heat loss from the surfaces in contact with the water-cooled copper mould was assumed to occur via the combined effects of conduction and radiation. The heat flux applied to the side and bottom surface was based on **Equation (4.19)**. The heat transfer coefficient, h_c, reported by Ritchie is shown in **Figure 4.14a** and was employed in this model. The surface tension coefficient reported by Ritchie [23] for "low sulfur" content (less than 10ppm) SS316is shown in **Figure 4.14b**. The surface tension coefficient is negative when the temperature is above 1700K.

Buoyancy, Marangoni forces, and mushy zone resistance were considered in the model by the momentum source term defined in **Equations (4.4)-(4.6),** respectively. The fluid flow boundary conditions include symmetry along the centerline ($u_r = 0$ @ r = 0) and front and back walls, no-slip conditions on the right side and bottom walls ($u_r = u_z = 0$ @ $r = R$ and $z = L$), and free slip conditions on the top surface ($u_z = 0$ @ z = 0).

The steady solution was solved using a transient formulation in which the simulation was run until steady-state conditions were reached. A uniform temperature of 1700 K and velocity

of 0 m/s were applied to the domain as initial conditions.

Figure 4.15 compares the predicted pool shape with that observed experimentally. The green and blue lines represent the liquidus and solidus isotherms, respectively. In both cases, the model results show liquid flowing from the center line along the top surface to the outer edge of the liquid pool. The predicted width and depth of the liquid pools for both the diffuse and focused beam cases are similar to the experimental measurement. Note the significant loss of material from the liquid pool resulting from evaporation. The analysis domain was chosen to be consistent in height with the distance between the top of the liquid pool and bottom of the button at the centre at the end of the experiment when the power was turned off and the liquid pool solidified. It was felt that this would better be able to simulate the conductive transport through the button at the centerline to the water-cooled copper mould and therefore would be able to more accurately predict the pool depth.

The difference in the liquid pool shape at the outer radius in the focused beam case may be a result of the sign change of surface tension coefficient of SS316 at low temperatures as well as the compositional change due to evaporation resulting in an overestimation of the downward flow at the outer radius of the pool.

Figure 4.16 compares the predicted top surface temperature profile with that measured using an NIR camera for both the diffuse and focused beam cases. The predicted temperatures show good agreement with the measurements in the liquid region of the top surface for the diffuse beam case (**Figure 4.16a**). The predictions also appear to be in good agreement in the focused beam case for the outer 2/3 of the liquid pool radius. However, the predictions and measurements appear to be diverging somewhat toward the centre of the liquid pool although

the measured data from the centre was not available. The comparatively poorer agreement in the solid is likely a consequence of the difference in emissivity between the solid and liquid given that the camera was calibrated based on the solidification (liquidus) temperature.

Overall, the model adequately predicts the depth and width of the liquid pool. The predicted surface temperatures show good agreement with the experimental data in the liquid regions. Thus, the coupled thermo-fluid flow modeling approach described in this chapter has been validated and the method of including Marangoni flow is correct and can be used in the further modeling of electron beam button melting process for Ti-6Al-4V.

Table 4.1 Materials properties of Ti-6Al-4V

Property	*Symbol*	*Value*	*Units*
Density	ρ	*Refer to Fig. 4.2*	kg m^{-3}
Specific heat	C_p	*Refer to Fig. 4.2*	J kg^{-1} K^{-1}
Conductivity	k	*Refer to Fig. 4.2*	W m^{-1} K^{-1}
Viscosity	υ	0.003	Pa s
Surface tension coefficient	$\partial\sigma/\partial T$	-0.00027	N m^{-1} K^{-1}
Liquidus temperature	T_l	1625	ºC
Solidus temperature	T_s	1595	ºC
Latent heat of solidification	$L_{l\rightarrow s}$	286000	J kg^{-1}
Latent heat of α/β trans.	$L_{\alpha\rightarrow\beta}$	48000	J kg^{-1}
Emissivity	ε	0.4	-

Table 4.2 Parameters for thermal boundary condition for EB button melting of Ti-6Al-4V

Property	*Symbol*	*Value*	*Units*
Beam power	P_w	12000	W
Standard Deviation	r_σ	0.008	m
Chamber Temperature	$T_{chamber}$	25	ºC
Mould Temperature	T_{mold}	25	ºC
Stefan-Boltzman constant	σ	5.67×10^{-8}	W m^{-2} K^{-4}

Table 4.3 Material properties of water used in subroutine validation test

Density	997 kg m^-3
Specific heat	4181.7 J kg^{-1} K^{-1}
Viscosity	0.0008899 Pa s
Thermal Conductivity	0.6069 W m^{-1} K^{-1}

Table 4.4 Physical properties of SS316 [23]

Viscosity	0.005 Pa s
Liquidus temperature	1673 K
Solidus temperature	1643 K
Latent heat of fusion	2.7×10^{5} J kg^{-1}
Latent heat of evaporation	7.455×10^{6} J kg^{-1}
Emissivity	0.3

Table 4.5 Processing parameters for SS316 button model [23]

Beam power	5440 W
Beam focal radius	0.003,0.025 m
Beam location radius	0 m
Ambient temperature	300 K
Mould temperature	300 K

Table 4.6 Mass fractions and activity coefficients of alloying elements in SS316 [23]

Element i	*Mass fraction*	γ_i
Cr	0.1739	1.0
Fe	0.6755	1.0
Ni	0.1298	0.67
Mo	0.0208	1.0

Table 4.7 Coefficients for calculating saturated vapour pressures of alloys elements in SS316 [23]

Element i	*A*	*B*	*C*	*D*
Cr	20680	1.31	0	14.56
Fe	19710	1.27	0	13.27
Ni	22400	2.01	0	16.95
Mo	32842.5	0.236	0.145	11.018

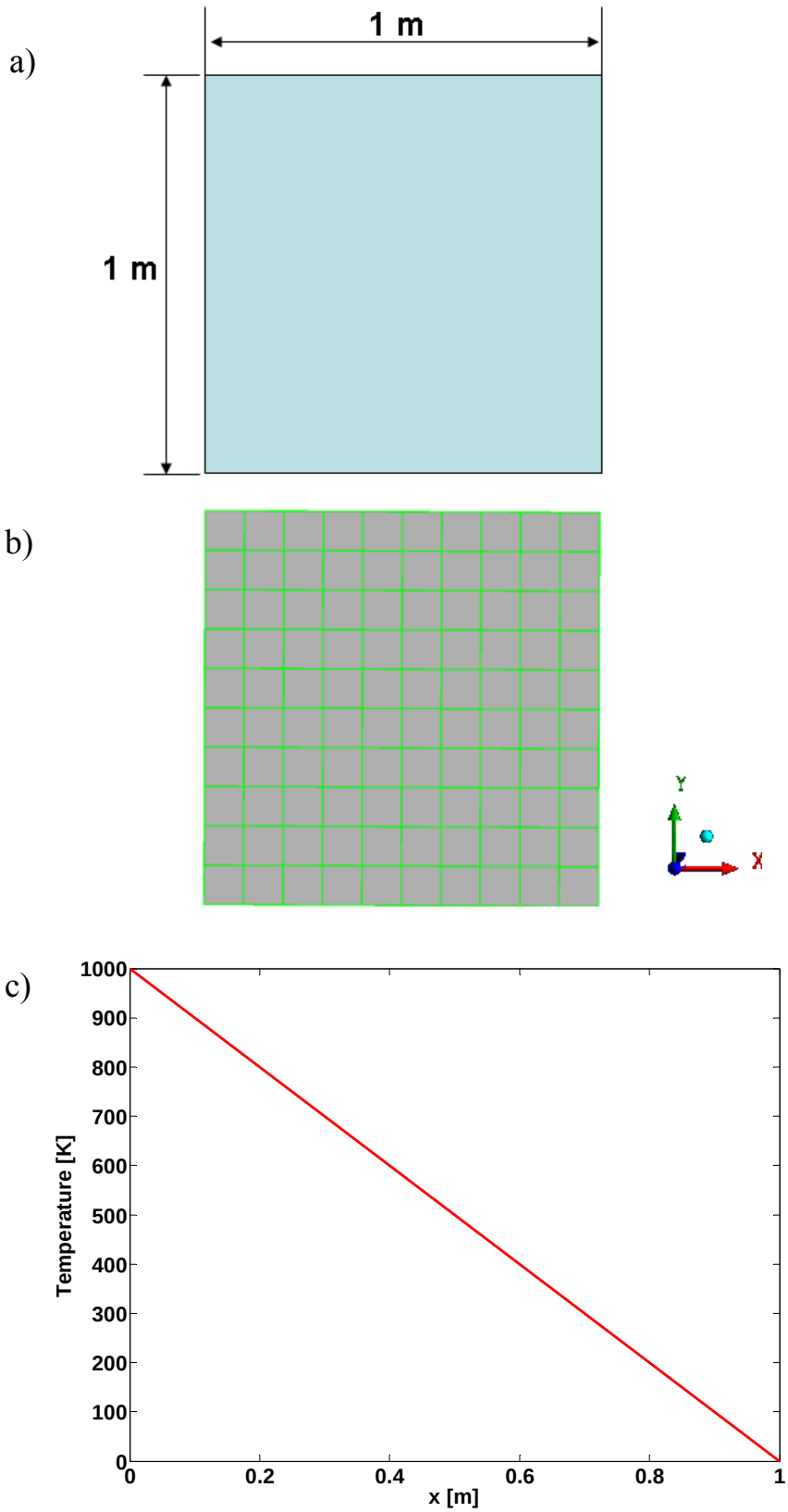

Figure 4.1 a) Geometry, b) mesh, and c) temperature change with distance in x direction for Marangoni subroutine validation test

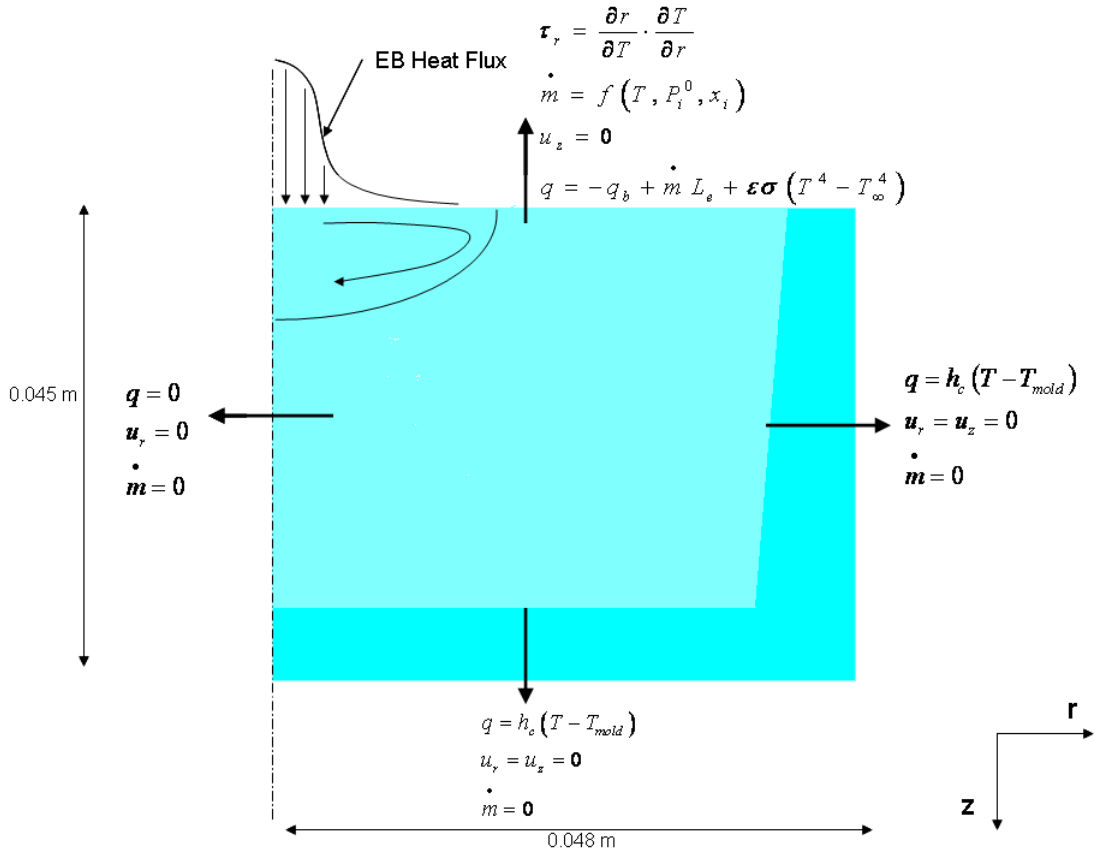

Figure 4.2 Geometry and boundary conditions applied to a model of EB button melting of SS316

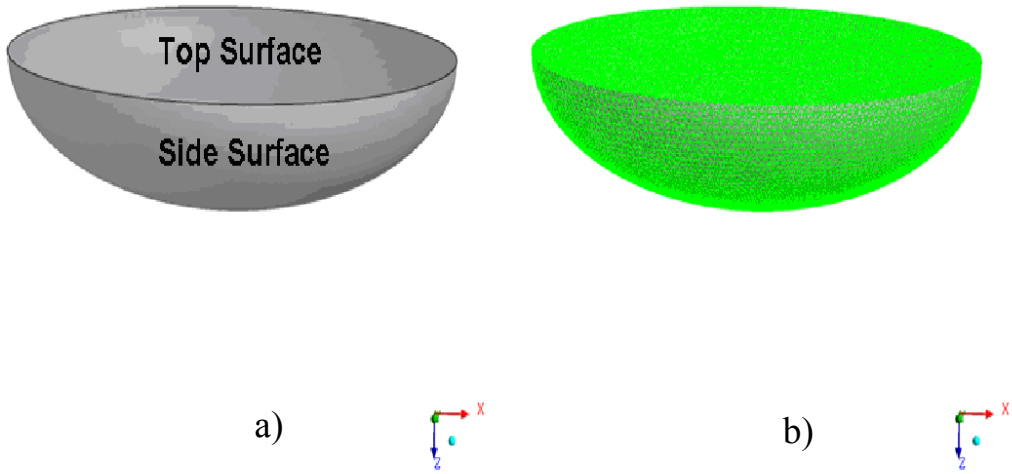

Figure 4.3 a) Geometry and b) mesh of the EB button model for Ti-6Al-4V

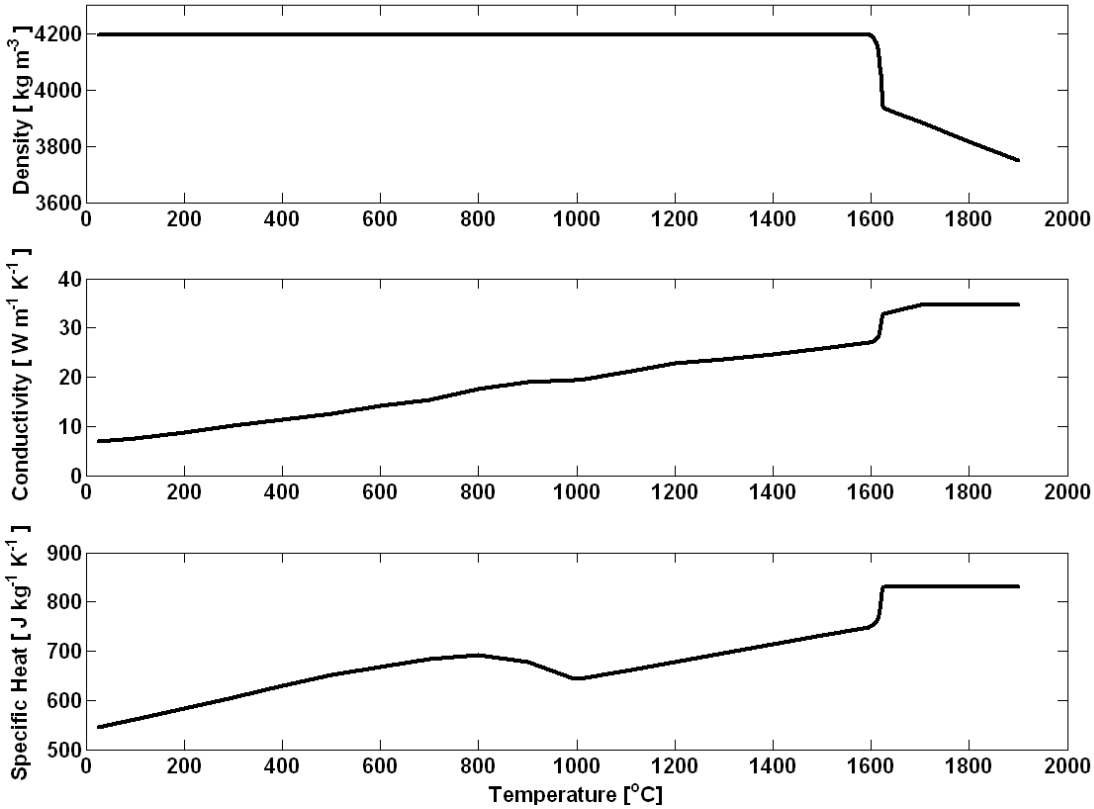

Figure 4.4 Density, conductivity and specific heat of Ti-6Al-4V as a function of temperature

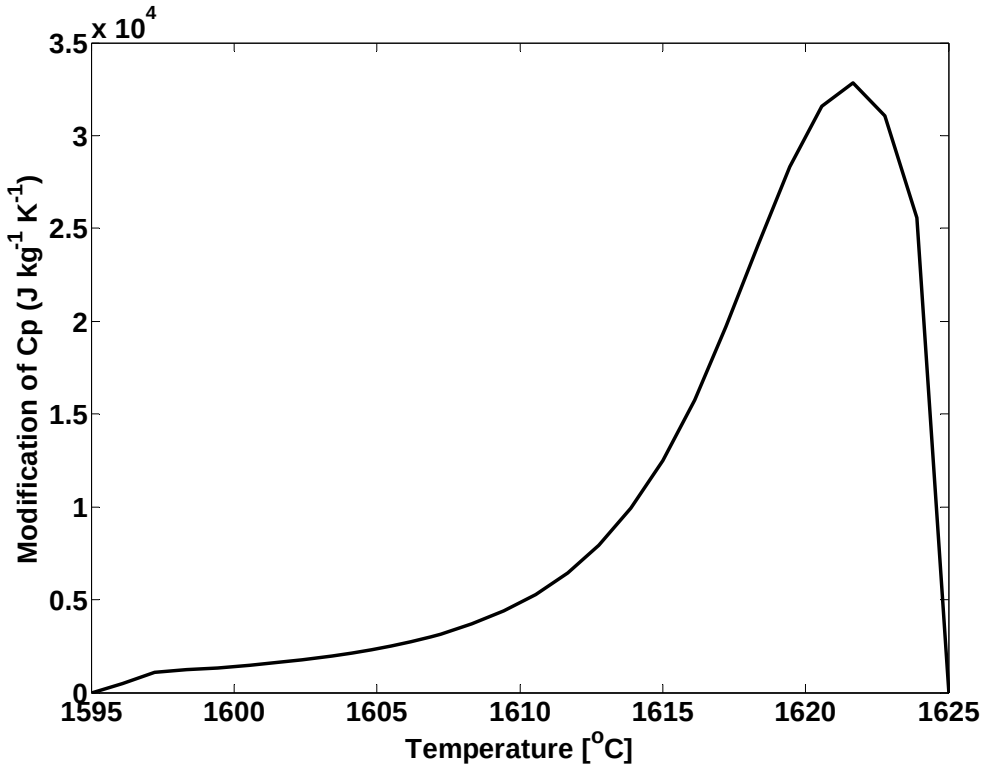

Figure 4.5 Additional specific heat component for the liquid-to-solid transformation

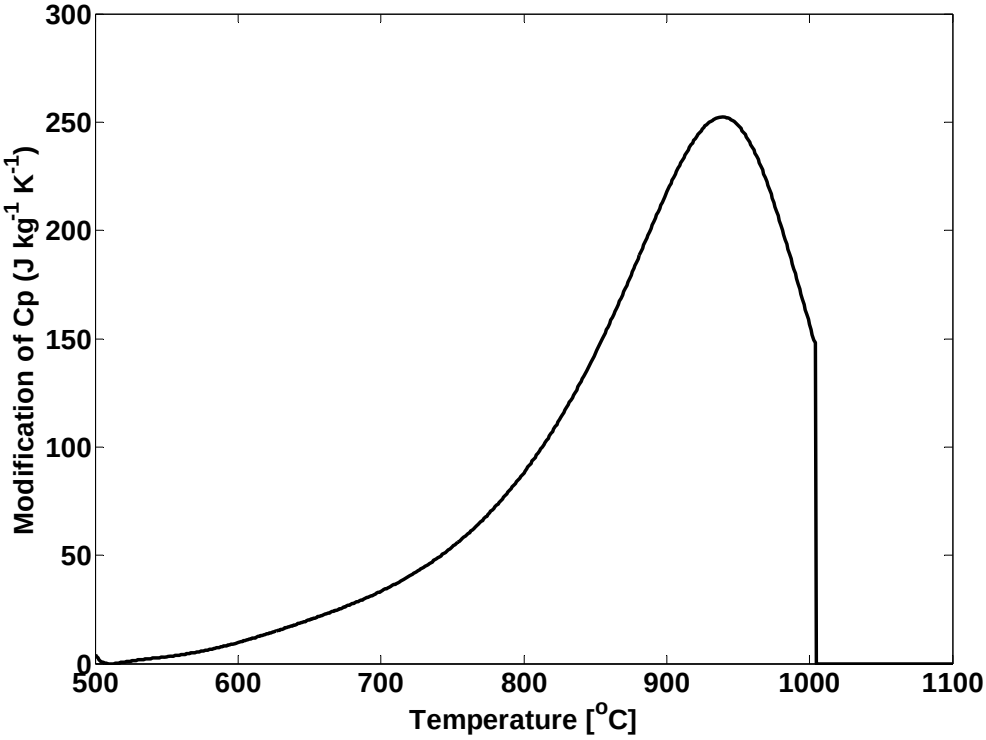

Figure 4.6 Additional specific heat component for the β/α transformation

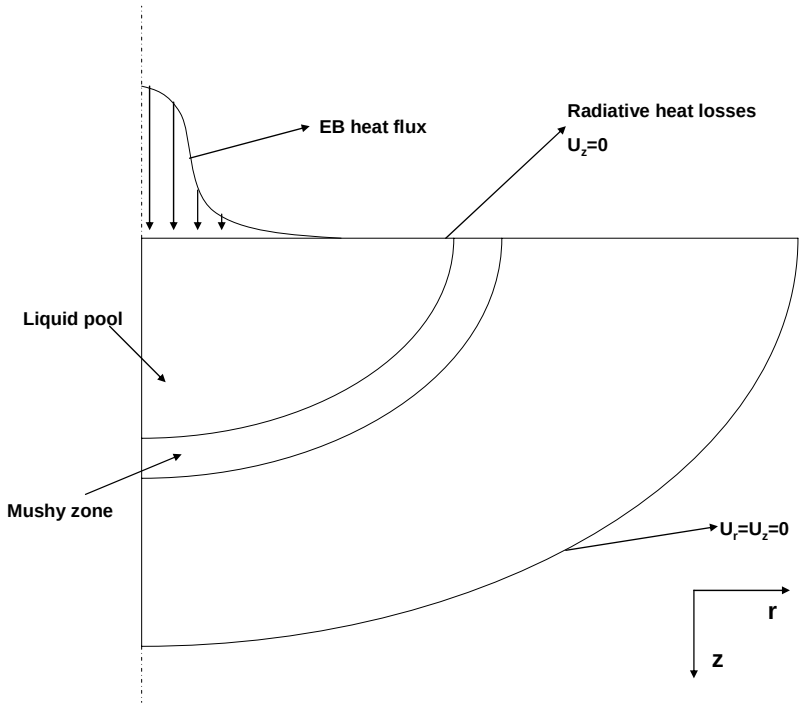

Figure 4.7 Boundary conditions applied to the EB button melting

a)

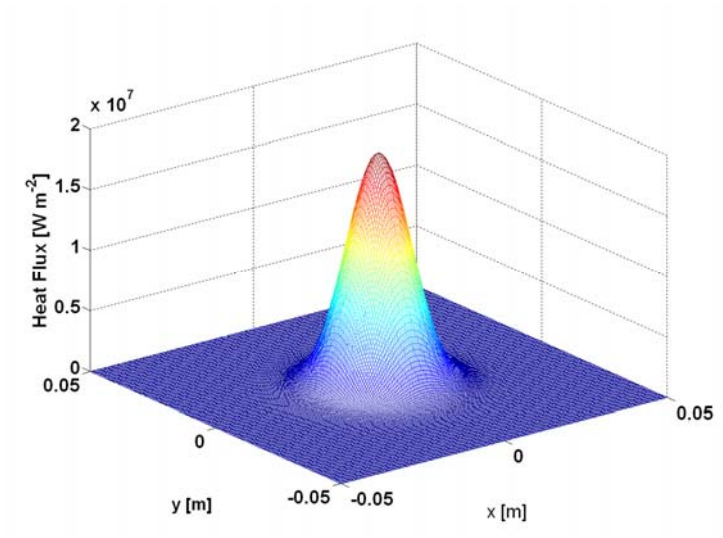

b)

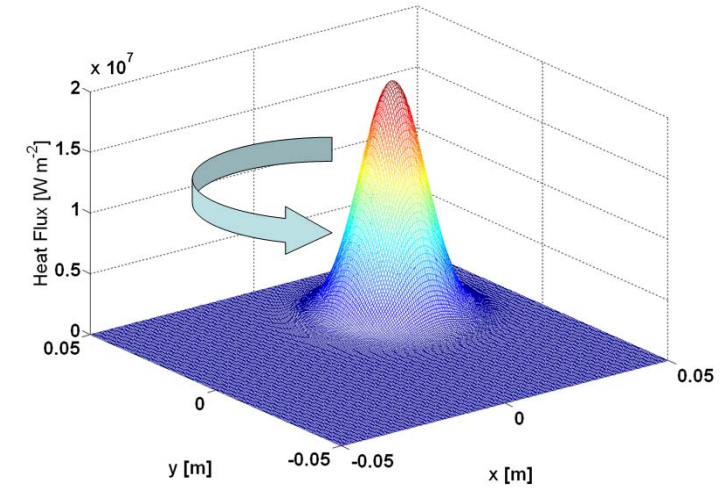

c)

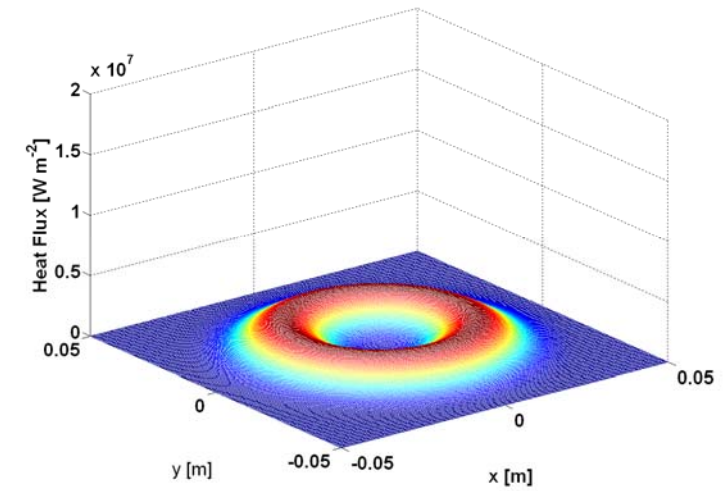

Figure 4.8 Heat flux distributions for three electron beam cases: a) centered, b) moving EB, and c) time-averaged

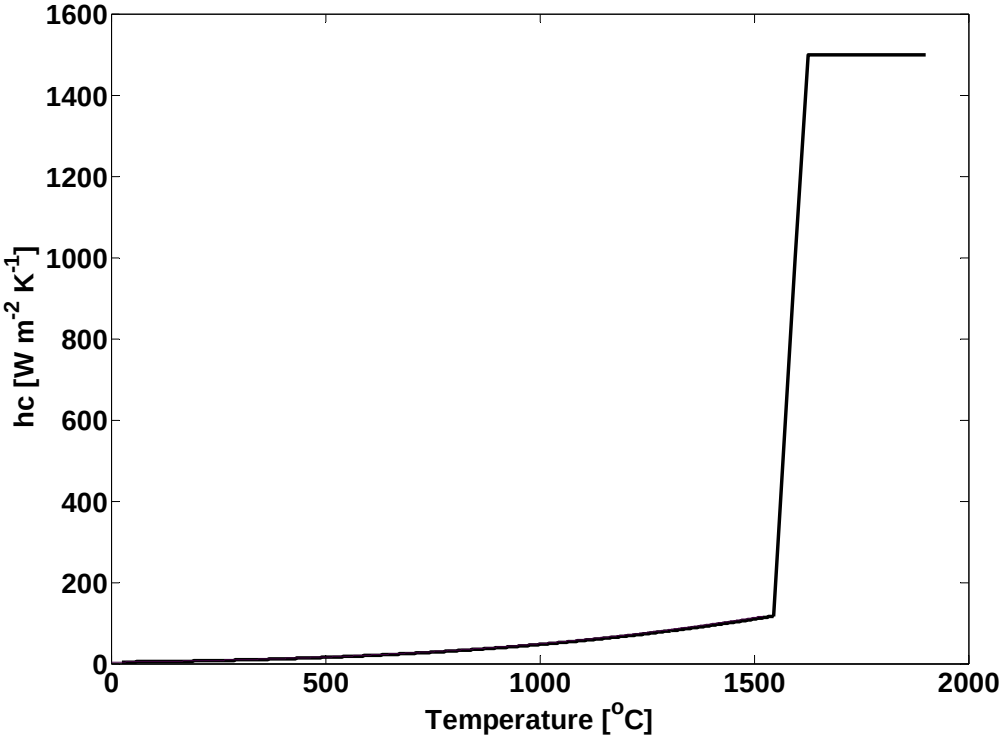

Figure 4.9 Heat transfer coefficient applied to the side surface

a)

b)

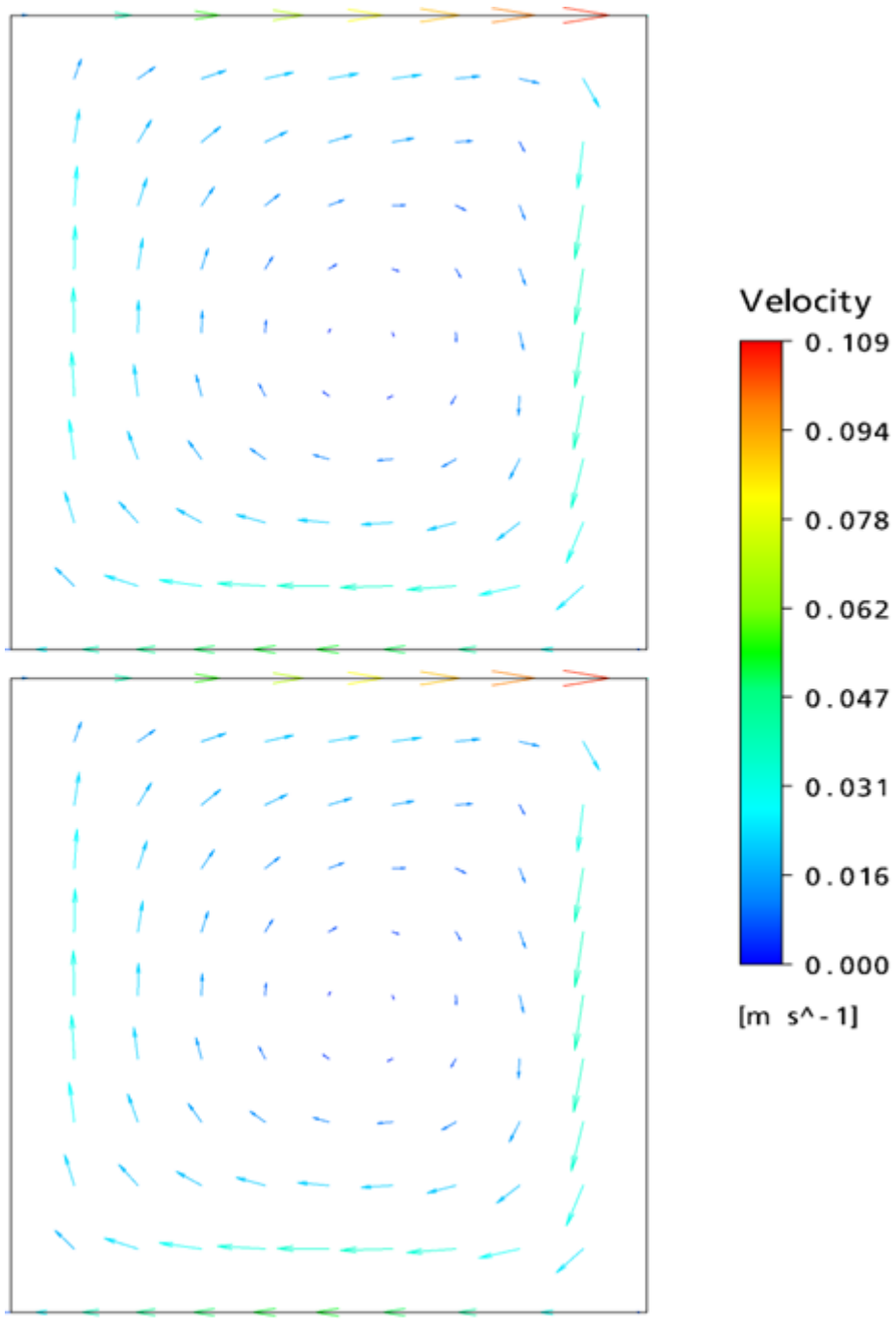

Figure 4.10 Velocity vector plot of water flow prediction for a) Marangoni force applied via subroutine and b) Marangoni force calculated manually and applied directly in CFX

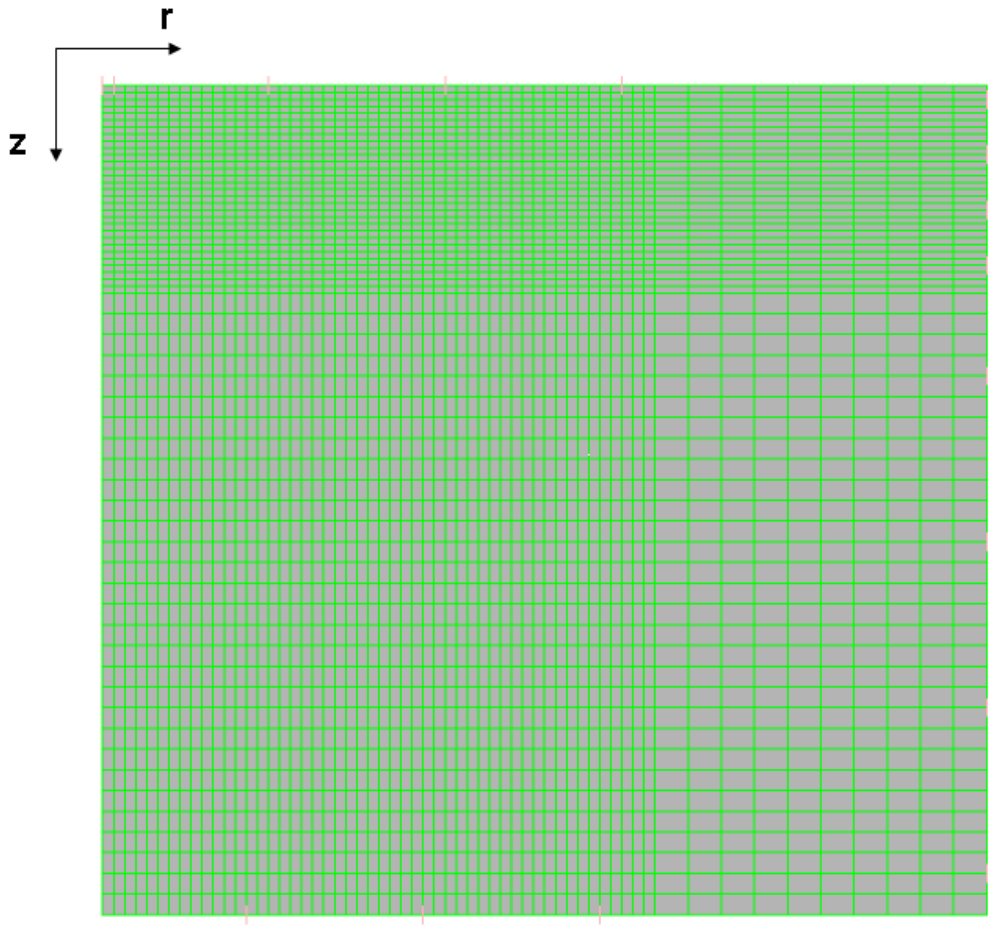

Figure 4.11 Grid of 60 × 60 cells used for the EB button melting model of SS316. Left side is axis of the symmetry

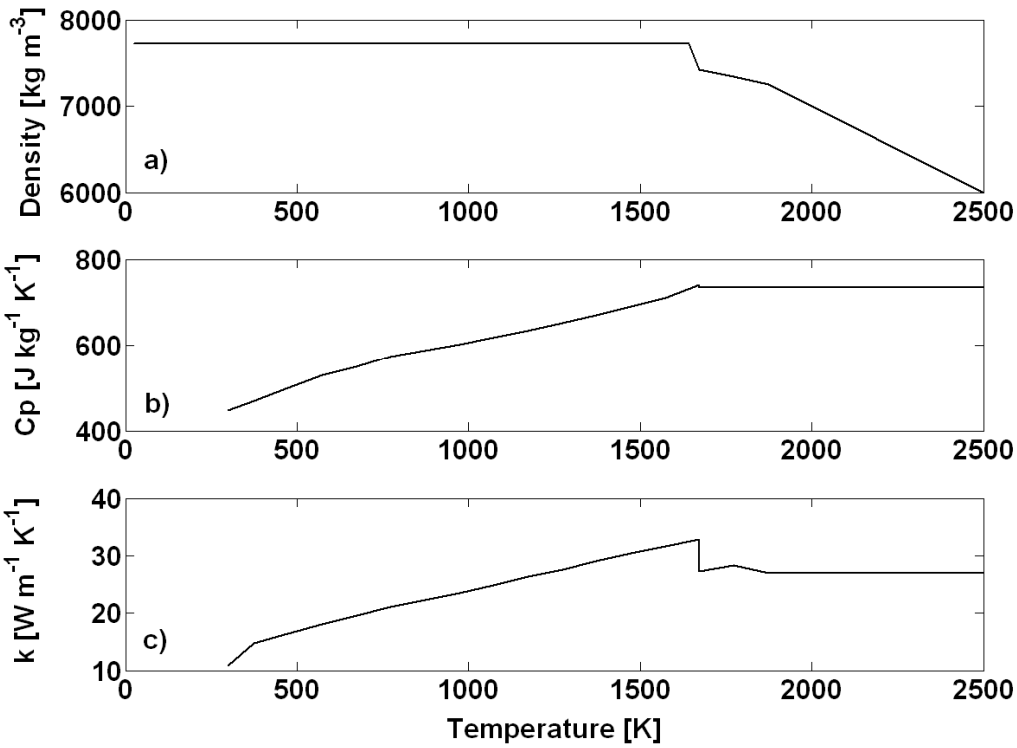

Figure 4.12 Materials properties of SS316 as a function of temperature: a) density; b) specific heat; c) thermal conductivity [23]

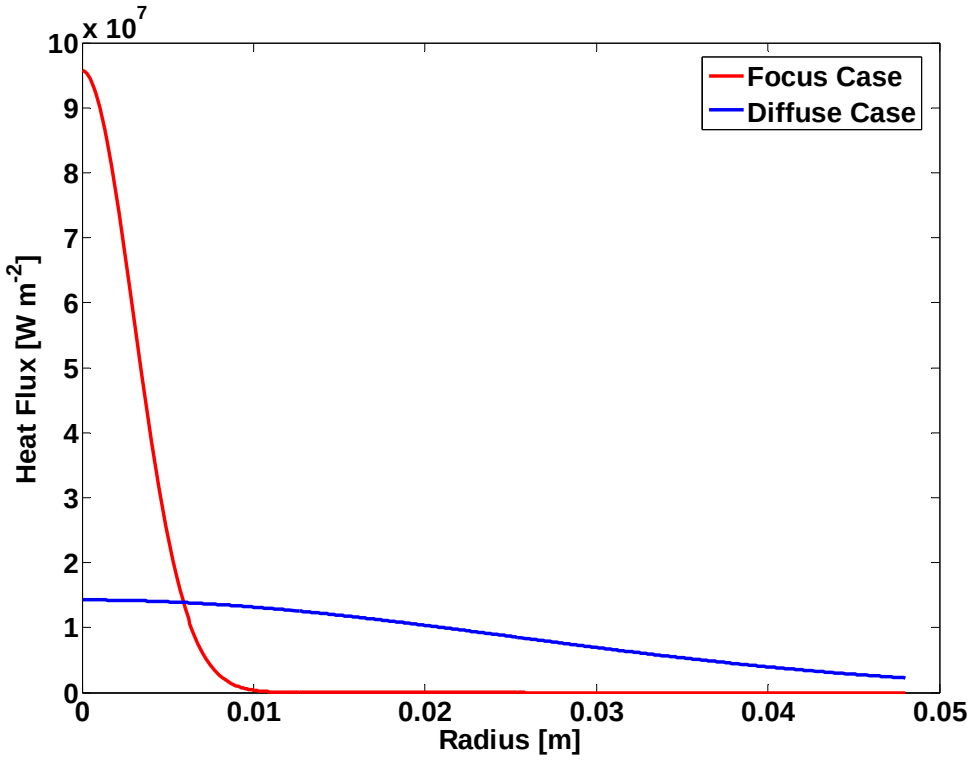

Figure 4.13 Heat flux distributions applied in SS316 button model for diffuse and focused electron beam heating conditions

a)

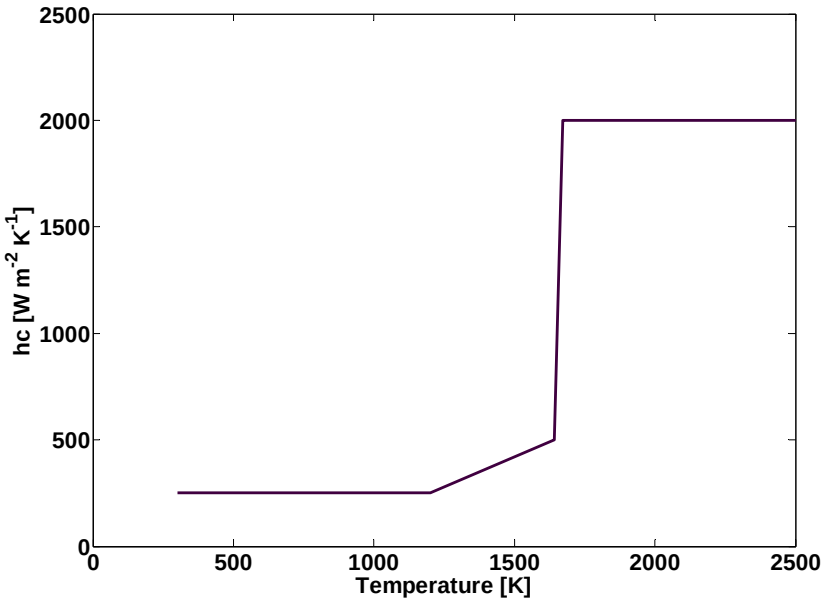

b)

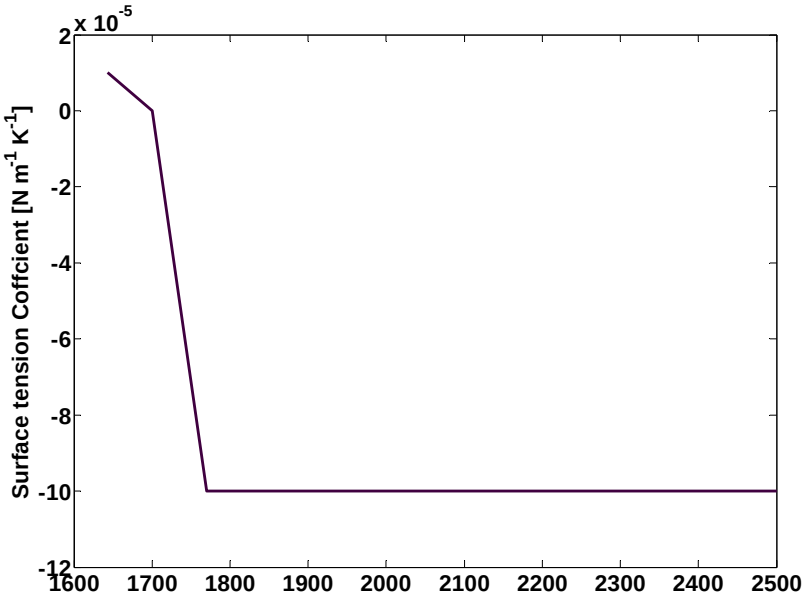

Figure 4.14 a) Heat transfer coefficient applied at the mould contact area and b) surface tension coefficient for low (10 ppm) sulfur level given as a function of temperature [23]

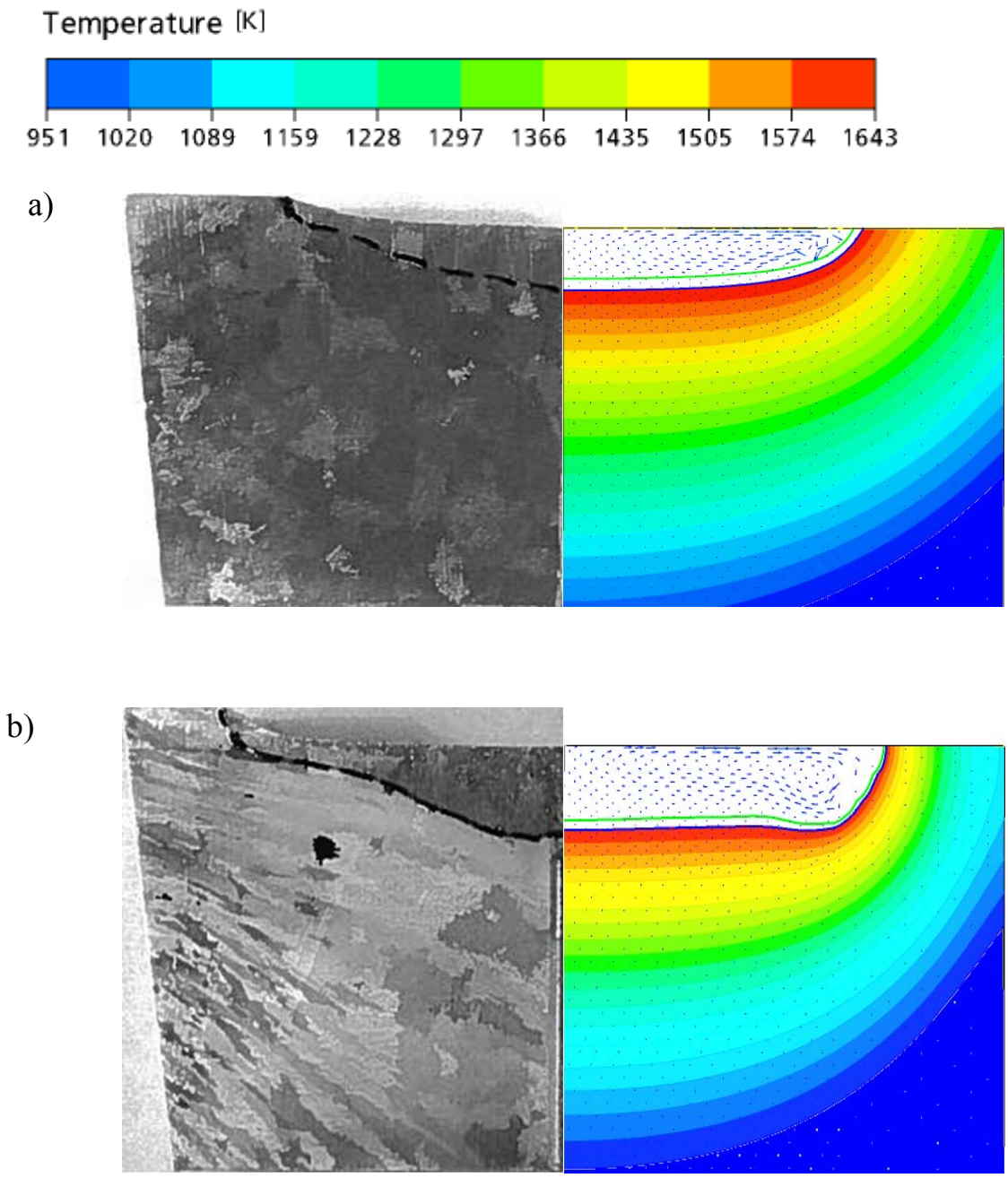

Figure 4.15 Comparison between predicted solid-liquid interfaces with cross section photographs [23] for two beam focus cases: a) diffuse beam and b) focused beam. Velocity vectors in the liquid, temperature contours up to the solidus temperature in the solid. Liquidus (green) and solidus (blue) isotherms overlaid

a)

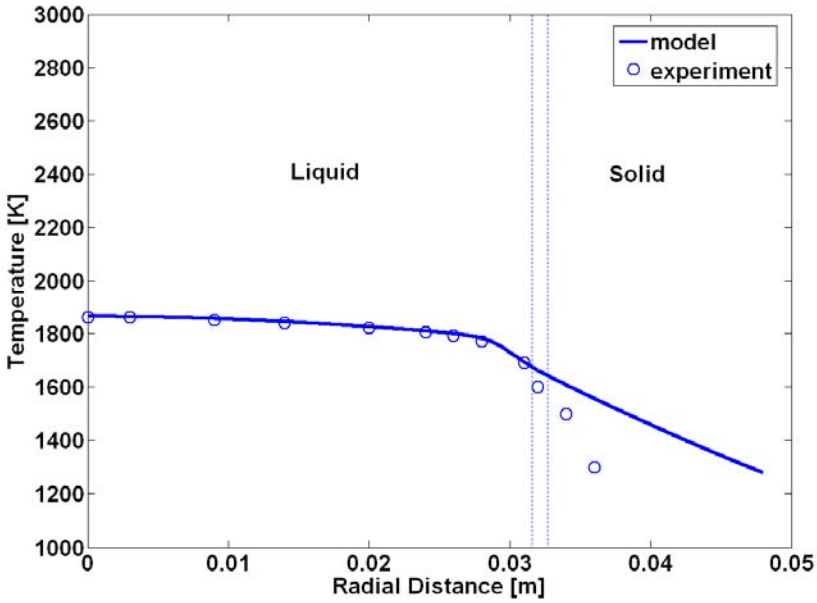

b)

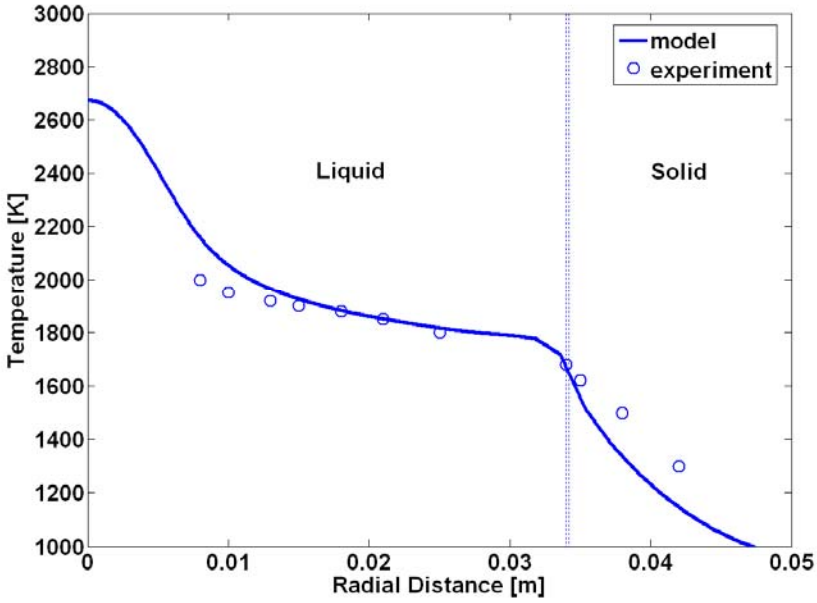

Figure 4.16 Comparison of the predicted and measured (via an NIR camera) surface temperatures for: a) diffuse beam, and b) focused beam cases (experimental data from Ritchie's thesis [23])

5 Results and Discussion

In this chapter, the results of the model applied to EB button melting of Ti-6Al-4V are presented. A centered, stationary EB heating condition has been used to investigate the effects of Marangoni, buoyancy, and flow resistance within the mushy zone on heat transfer and fluid flow in the button. Following this, the model will be used to investigate different methods to describe a moving EB source. Finally, a sensitivity analysis will be performed with the model using a centered EB heating condition to assess the sensitivity to changes in a couple of key numerical and process parameters.

5.1 Centered EB Heating

The EB button model was used to predict the effects of heating using a stationary electron beam located at the center of the top surface. The beam power (P_w =1.2 kW) and focus (r_σ = 8 mm) for this case were selected to produce a reasonable liquid pool within the button. To begin, a series of model runs were preformed with and without the source terms identified in Chapter 4.

The predicted temperature distributions on cross-sections of the button for stationary, centered EB heating with: a) no momentum sources, b) only Marangoni force, c) only buoyancy force, d) Marangoni and buoyancy forces, e) Marangoni and Darcy forces, and f) Marangoni, buoyancy, and Darcy forces are presented in **Figure 5.1**. Lines representing the liquidus (red) and solidus (blue) isotherms have been superimposed on the contour images to delineate the liquid pool. The flow fields within the liquid for the same conditions presented in **Figure 5.1** are shown in **Figure 5.2**. In **Figure 5.2**, the vectors indicate the orientation of the flow and the velocity magnitude is indicated by both the vector length and color.

As can be seen in **Figure 5.2a**, there is no flow observed in the predictions for the model without momentum sources, even though the full Navier-Stokes equations are solved. The absence of a driving force for flow results in no flow and conditions that are analogous to a conduction-only model where the contours of temperature (**Figure 5.1a**) decrease in a manner determined by the diffusion of heat through the liquid and solid.

When only Marangoni flow is considered (**Figure 5.2b**), flow on the top surface is directed outward radially and downward along the solid liquid interface resulting in symmetric recirculating cells. The liquid pool in the button becomes wider and shallower due to enhanced heat transfer radially outward along the top surface associated with the advective transport of heat.

The predicted temperature fields on a cross-section of the button with buoyancy only and with both buoyancy and Marangoni forces are presented in **Figure 5.1c** and **d**, respectively and the associated flow fields are presented in **Figure 5.2c** and **d,** respectively. When only buoyancy forces are considered, the liquid that is cooled along the solid liquid interface sinks due to the density increase with decreasing temperature. To conserve volume, there is a corresponding volume of liquid that rises to the surface in the center and then outward radially. The effect of buoyancy is similar to that of including surface tension driven (Marangoni) flow, in that both result in symmetrical recirculating flow that enhances radial heat transport on the top surface. Under the conditions examined with the model, the effect of buoyancy appears larger as the pool is shallower and more spread out. The combined effect of Marangoni and buoyancy forces (**Figure 5.1d** and **Figure 5.2d)** results in a slight spreading of the liquid pool compared to buoyancy only case.

The predicted temperature distribution on a cross-section of the button for the centered beam case with both Darcy and Marangoni forces included is presented in **Figure 5.1e** and the associated flow field is presented in **Figure 5.2e**. The liquid pool is narrower and deeper compared to the case considering only Marangoni forces (**Figure 5.1b** and **Figure 5.2b)**. Thus, the introduction of a resistance to flow in the mushy zone (Darcy force) decreases the downward flow adjacent to the solid/liquid interface resulting in a reduction in the recirculating flow and the associated outward radial flow of heat along the top surface (**Figure 5.2f)**. This effect can be more clearly seen in the predicted temperature distribution on a cross-section of the button where all three forces are included (**Figure 5.1f**). The resistance to flow provided by the Darcy force reduces the Marangoni induced flow near the periphery of the top surface and buoyancy driven flow along the solid/liquid interface.

To further explore surface tension driven flow, the sign on the surface tension coefficient was changed from negative, which is the case for Ti-6Al-4V, to positive. The results for the two cases are presented in **Figure 5.3**. As in the previous results, a stationary EB centered on the top surface has been applied. Buoyancy and mushy zone flow dampening were not included in the momentum source term to highlight the effects of surface tension forces. The temperature contours above the solidus temperature have been removed and the flow vectors have been overlaid. When the surface tension coefficient is negative (**Figure 5.3a**), flow is directed outward along the top surface and a corresponding recirculating flow cell develops, which results in a wider and shallower liquid pool. The maximum velocity occurs near the mid-radius. When the surface tension coefficient is positive (**Figure 5.3b**), the flow on the top surface is directed inward resulting in a corresponding downward flow at the centerline that

re-circulates outward at the bottom of the button, opposite in direction to previous case. The liquid pool becomes narrower and deeper compared to the pool predicted with a negative surface tension coefficient. Changing the surface tension coefficient from a negative to positive value increases the maximum temperature by 400 K. Thus, in the absence of other momentum source terms, the sign of the surface tension coefficient dramatically affects the flow patterns, temperature distribution within the liquid and solid, and the size and shape of the liquid pool.

In addition to the sign on the surface tension coefficient, the effect of varying the surface tension coefficient magnitude over a range from 0 to $-4x10^{-4}$ $kg{\cdot}s^{-2}{\cdot}K^{-1}$has also been assessed by plotting the temperature profile on the top surface along a straight line from the center to the outer edge of the button for the different cases. The results are shown in **Figure 5.4**. Stationary, centered, EB heating was applied and only Marangoni forces were included in the momentum source term. Generally, in all of the cases examined the temperature profile shows a decrease with increasing distance from the center. The greatest difference in temperature between the centre and outer radius (3100 K vs. 1750 K) is predicted when the surface tension coefficient is zero (analogous to conduction-only case). For non-zero surface tension coefficients, the temperature at the center decreases due to enhanced advective transport of heat radially outward, which leads to a corresponding increase in temperature near the mid-radius and a moderate increase near the outer radius. The magnitude of the temperature drop at the center is shown to increase when increasing surface tension coefficient. The largest change in the temperature profile is realized on changing the coefficient from 0 – e.g. no Marangoni driven flow - to a value of $-1.0 \times 10^{-4}kg{\cdot}s^{-2}{\cdot}K^{-1}$. The effect of further increases

in the magnitude become incrementally smaller over the range examined and appears to saturate as the surface tension coefficient approaches -4x10^{-4} kg·s^{-2}·K^{-1}.

During EB melting of Ti-6Al-4V, the evaporation of aluminum may lead to a change in surface tension because the surface tension of aluminum is smaller than that of titanium [46, 47]. As the current version of the model does not track compositional changes due to evaporation, the variation of surface tension due to evaporation of aluminum was not considered. A surface tension coefficient value of -2.7 x10^{-4} kg·s^{-2}·K^{-1} based on Kelar's paper [22] has been used in remainder of this investigation.

5.2 Non-stationary EB Heating

The model was used to predict the temperature and velocity distributions in the button for non-stationary EB heating where the beam traces a circle with a diameter of 50 mm on the top surface. As in the previous case, the beam power was set to P_w = 1.2 kW and focus r_σ = 8 mm for the analysis. The Marangoni, buoyancy and Darcy forces are all included as momentum source terms in this analysis. Referring to **Figure 4.8b** and **c**, two approaches for modeling the EB heat input were investigated: i) a resolved, moving heat flux boundary condition, in which the beam sequentially moves from one spot to the next to form a circular pattern on the surface that is repeated with a given frequency; and ii) a time-averaged heat flux boundary condition. For the moving heat flux boundary condition, the model was run to cyclic steady state, where the temperature and velocity distributions vary as function of time, but are constant relative to beam position – e.g. the temperature is invariant at a point on the surface at a given time in the beam pattern cycle. A cycle consists of a series of 256 points, each representing a point on the circumference of the circle where the beam spot dwells for a time

equal to $\frac{1}{F \cdot 256}$ s, before moving on to the next spot in the sequence along the circle circumference, where F is the beam pattern repetition frequency. The beam frequency used at TIMET is applied as the standard frequency in the current research, which will not be provided due to a confidentiality agreement.

Figure 5.5 shows the predicted temperature distribution on the top surface of the button for the moving heat flux and the time-averaged heat flux cases. In the case where a moving heat flux boundary condition was applied (**Figure 5.5a**), a peak temperature of 2620 K occurs near the location of the center of the EB heat flux distribution. Away from the beam location, the temperature decreases to an average value of ~2000 K. The direction of beam motion is evident by the trail of higher temperature liquid that follows the beam. The large surface temperature gradients would lead to comparatively large Marangoni forces in directions away from the EB location.

For the time-averaged heat flux EB case (**Figure 5.5b**), there is a higher temperature (~2100 K) region consistent with the path that the beam traverses, with areas of lower temperature present both inside and outside the beam pattern. The low temperature gradients in the time-averaged case would result in comparatively moderate Marangoni forces.

Contour plots of the velocity magnitude on the top surface of the button for the moving heat flux and time-averaged heat flux cases are presented in **Figure 5.6**. The highest velocities (~0.04 $m \cdot s^{-1}$) are observed in the moving heat flux case (**Figure 5.6a**) in the vicinity of the EB where the temperature gradients and associated Marangoni forces are highest. Away from the EB, the velocity decreases due to the reduced temperature gradients. In the time-averaged case (**Figure 5.6b**), the velocity is near zero at the location of the beam path due to zero

temperature gradient. The highest velocity is seen on the outer edge adjacent to the mould where the highest temperature gradients exist.

The pool profile and flow field on a vertical plane bisecting the button for the moving heat flux and the time-averaged heat flux cases are compared in **Figure 5.7**. The velocity contours for the moving heat flux case (**Figure 5.7a**) shows that the local surface heating results in the development of a localized recirculating flow field. The time that the beam spends at a particular location results in both a localized hot spot on the surface and the development of recirculating flow cells under the beam spot – e.g. there is what appears to be an off-centre recirculating cell formed on either side of the beam spot – whereas in the time averaged case the recirculating cell that develops is larger in size and symmetric with respect to the liquid pool. One consequence of this difference is that the liquid isotherms in the two cases have slightly different shapes. Notably the profile in the time-average case has a slight discontinuity in the curvature at approximately the ¼ radius location associated with the formation of the stable recirculating cells. Based on **Figures 5.5 – 5.7**, the main difference between the two cases examined relates to the surface temperature and surface velocity fields, whereas the pool profile appears to be virtually uninfluenced by the approach used to model the moving beam.

To further explore the influence of EB pattern cycle time, the model has been run with beam pattern cycle times of 0.1, 1, 5 and 10 s (frequencies of 10, 1, 0.2, and 0.1 Hz) in addition to the standard case. Thermal contours of the top surface and on a vertical plane bisecting the button are plotted in **Figures 5.8** and **5.9** for cycle times of 0.1, 1, 5 and 10 s. Velocity contours of the top surface and on a vertical plane bisecting the button are plotted in

Figures 5.10 and **5.11** for cycle times of 0.1, 1, 5 and 10 s. **Figure 5.11** also includes the flow vector plots on the vertical plane bisecting the button for the different beam cycle times examined.

Turning first to **Figure 5.8,** when the beam cycle time is 0.1 s (**Figure 5.8a**), the temperature distribution on the top surface is very close to the case for the time-average EB heating (**Figure 5.5b**). The peak temperature observed on the surface is ~2100K and is located within a circular band of approximately uniform temperature consistent with the path traced by the beam. When the beam cycle time is increased to 1s (**Figure 5.8b**), the pattern of temperature on the liquid surface changes noticeably to one in which the location of the beam spot becomes apparent. The temperature distribution loses its radial symmetry and the highest temperature increases to around ~2600 K, located approximately at the center of the beam spot. Away from the location of beam center, the temperature decreases to ~2100 K. As the beam cycle time is increased to 5 and 10 s, **Figure 5.8c** and **Figure 5.8d**, respectively, the localized heating associated with the beam spot becomes intensified resulting in peak temperatures ~2900 K and ~3100 K respectively. Furthermore, the temperature contours around the beam spot become more symmetric and there is less evidence of a "tail" of hot liquid behind the beam spot.

Turning to the contours on the vertical plane bisecting the button, shown in **Figure 5.9**, lines have been added to delineate the liquidus isotherm (red) and the solidus isotherm (yellow). The key observation is that despite increased localization of heating under the beam spot, with increasing cycle time, there is relatively little effect on the liquid pool profile and depth. The results suggest a slight reduction in the depth of the liquid pool and "flattening out" of the

isotherms with increasing cycle time.

The contour plots of the velocity magnitude presented in **Figure 5.10** show an intensification of the flow field on the surface surrounding the beam spot with increasing cycle time. The flow field for the 0.1 s case is approximately the same as the time-averaged heating case (**Figure 5.6b**) and exhibits a high degree of radial symmetry. For the cycle times of 5 s (**Figure 5.10c**) and 10 s (**Figure 5.10d**) the symmetry is lost and the flow field is dominated by a region of relatively intense flow immediately ahead of the beam spot consistent with the location of the largest temperature gradients (see **Figures 5.8c** and **d**).

The contour plots showing the velocity magnitude and orientation presented in **Figure 5.11** for the different cycles reinforces the observation that there is a gradual intensification of the flow and loss of radial symmetry with increasing cycle time. Symmetric recirculating flows are observed for 0.1 and 1 s cycles times. By 5 s, there is a loss of symmetry in the flow pattern and the development of a recirculating cell under the beam spot. The difference between the 5 s and 10s cases appears to be that the recirculating cell formed under the beam spot is less localized to the vicinity of the beam spot for the 5s cycle time than for the 10s cycle time.

In order to further explore the effect of beam cycle time, the temperature and velocity at a series of radial locations has been averaged circumferentially and plotted as a function of radius. The resulting profiles of temperature and velocity are shown in **Figure 5.12 (a)** and **(b),** respectively. The dashed vertical line appearing on each plot indicates the center of the beam pattern. The error bars indicate the minimum and maximum temperature and velocity at a given radius for cycle times of 0.1 s (red) and 10 s (blue). Note: that there is a significant

range in temperature and velocity for the 10s cycle time in comparison to the 0.1 s cycle time associated with the longer beam spot dwell times (0.04 s vs 0.0004 s). There is also a transition in the temperature in the center region of the button as the cycle time is increased from 1 to 5 s. The increase in temperature at the centre that occurs at the change from 1 to 5 s corresponds to the breakdown in circumferentially symmetric flow pattern that results in a modest upward recirculating flow in the centre to one more dominated by the recirculating cells that form in proximity to the beam pattern. Overall, however, the circumferential averaged temperature profile does not show a high degree of sensitivity to beam cycle time, which is consistent with the lack of sensitivity that is also exhibited in the liquidus contour.

5.3 Sensitivity Analysis

A sensitivity analysis was conducted with the button model using stationary EB heating at the center of the top surface to determine the effect of changing numerical and process parameters. During model development, the results of the sensitivity analysis were used to help develop confidence in the veracity of the model and delineate the important model input parameters – e.g. those having the largest effect on the model.

5.3.1 Numerical Sensitivity

The sensitivity of the model predictions to variations in the numerical parameters of mesh size and time step have been evaluated. The choice of these two parameters often represents a tradeoff between accuracy and computational time with fine meshes and small time steps tending to result in better accuracy but longer execution times.

Mesh Size

The model was run with a series of meshes with decreasing maximum element edge

lengths. **Table 5.1** lists the maximum edge length, numbers of nodes and elements and maximum edge length ratio for the cases analyzed. **Figure 5.13** shows the temperature distributions on a cross-section of the button model predicted with the different mesh sizes. At a glance the results for the three meshes appear to be very similar. However, upon close inspection, there is some variation in the position of liquidus and solidus isotherms with mesh size. This difference is more easily seen in **Figure 5.14,** where the depth of the liquidus and solidus isotherms are plotted as a function of radius. The results indicate that both the medium and fine meshes (1 and 2 mm maximum edge length, respectively) yield similar results and the course mesh tends to over predict the depth of the liquid pool for approximately the centre 2/3 of the radius. As there were no significant differences between the 1 and 2 mm meshes, the 2mm maximum edge length mesh was chosen to save computational time while continuing to provide accurate results.

Time Step

The effect of time step size on the steady-state temperature distribution in the button was assessed. The model was run from the initial condition to steady-state with time steps of 0.1s, 0.25s, 0.5s, and 1s. The predicted temperature profiles for the different time steps are shown in **Figure 5.15**. The temperature distributions for time steps of 0.1s (**Figure 5.15a**) and 0.25s (**Figure 5.15b**) are similar. However, when the time step is raised to 0.5s (**Figure 5.15c**), the high temperature region near the center of the top surface tended to decrease in size and some instability in the isotherms within the liquid pool are apparent. Raising the time step further to 1s results in larger temperature distribution differences compared to the other cases. The depths of liquidus and solidus isotherms for the different time steps are plotted in the **Figure**

5.16. The profiles of the liquidus isotherms are nearly identical for time steps of 0.1 and 0.25s and the solidus isotherms appear unchanged for 0.1, 0.25 and 0.5s. Based on these results, a time step equal to 0.25s was selected for the thermal-fluid model.

5.3.2 Process Parameters

One obvious use for the model is to predict how changes to the model input parameters affect the liquid pool during EB melting of Ti-6Al-4V. To illustrate the use of the model for this purpose, a sensitivity analysis was conducted with the model to show the influence of the electron beam power and heat transfer coefficient on the shape of the liquid pool. The range of values used in sensitivity analysis is presented in **Table 5.2**.

The depths of the liquidus and solidus isotherms as a function of radius for different electron beam power and heat transfer coefficient are shown in **Figures 5.17** and **5.18**, respectively. As shown in **Figure 5.17**, increasing the beam power expands the size of the liquid pool. This results from increased power input and stronger Marangoni effects due to higher temperature gradients. Conversely, increasing the heat transfer coefficient，that is increasing the energy transferred to the mould, decreases the size of the liquid pool. For the range examined there is a larger difference realized by reducing the heat transfer coefficient than by increasing it relative to the base value.

5.3.3 Summary of Sensitivity Analysis

Table 5.3 summarizes the effect of the numerical, process and model input parameters examined on the maximum depth and width of the liquidus isotherm. The values reported in **Table 5.3** were calculated as the percent change relative to the results for the baseline parameters indicated.

Reviewing the changes made to the numerical parameters, there is less than a 1% difference in the liquid pool size except when the time step is 1s. Although changing a single parameter seems to have little effect, it should be noted that changes to multiple parameters may result in complex and significant effects. Process parameters such as electron beam power and heat transfer coefficient tend to have a larger effect on the liquid pool.

Table 5.1 Mesh data for the sensitivity analysis

	Coarse	Medium	Fine
Maximum Edge Length [mm]	5	2	1
Number of Nodes	5378	5520	21281
Number of Tetrahedral Elements	22060	24086	98179
Maximum Edge Length Ratio	12.9943	9.50899	9.37997

Table 5.2 Range of values for modeling process parameters used in sensitivity analysis

Property	*Symbol*	*Minimum*	*Value*	*Maximum*	*Units*
Electron beam power	P_w	9000	12000	15000	W
Heat transfer Coeff.	h_c	$f(T)\times 0.5$	$f(T)$	$f(T)\times 1.5$	W m^{-2} K^{-1}

Table 5.3 Summary of effects of parameters on the depth and width of the liquid pool used in sensitivity analysis

Change from *Baseline			Change Relative to Baseline	
			Depth (%)	Width (%)
Numerical Parameters	Maximum Mesh Size [mm]	5	+4.01	-0.345
		1	-0.430	0
	Time Step [s]	0.1	0	0
		0.5	-0.558	-0.603
		1	-0.912	-6.33
Process Parameters	Electron Beam Power [kW]	0.9	-24.23	-25.68
		1.5	14.56	28.20
	Heat Transfer Coefficient [W m^{-2} K^{-1}]	$f(T)\times 0.5$	19.58	24.23
		$f(T)\times 1.5$	-18.54	-13.44

* For Base line, maximum mesh size is 2 mm, time step is 0.25 s, electron beam power is 1.2 kW, and heat transfer coefficient is a function of temperature as shown in **Figure 4.9**

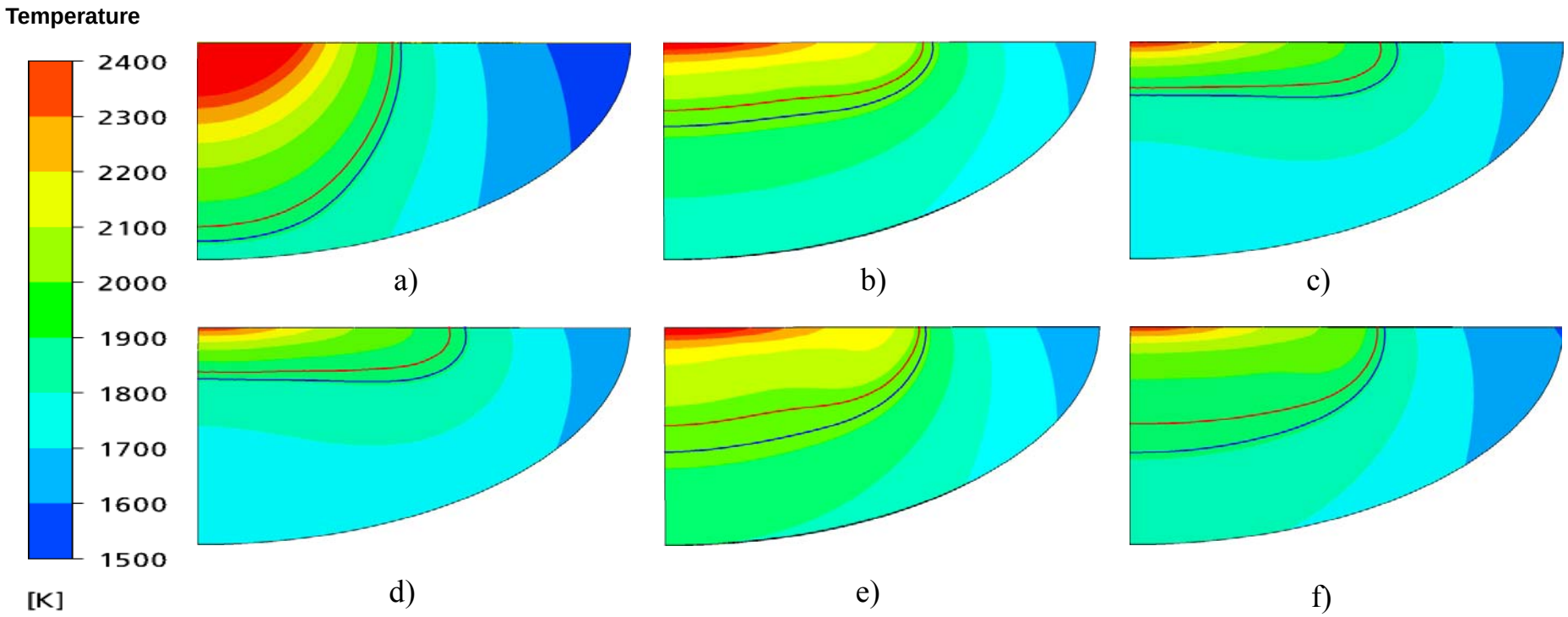

Figure 5.1 Predicted temperature distributions on cross-sections of the button model for stationary, centered EB heating with a) no momentum sources, b) only Marangoni force, c) only buoyancy force, d) Marangoni and buoyancy forces, e) Marangoni and Darcy forces, and f) Marangoni, buoyancy, and Darcy forces. Lines representing the liquidus (red) and solidus (blue) isotherms superimposed on contour images

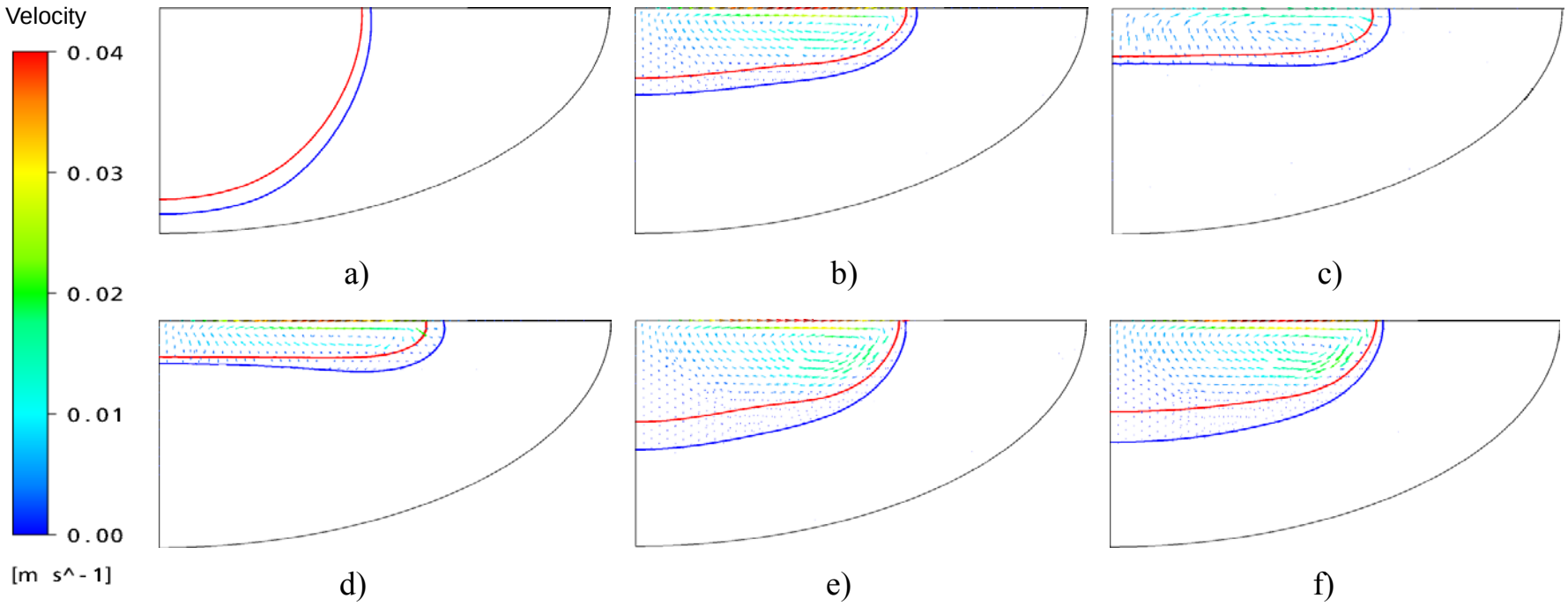

Figure 5.2 Predicted velocity vector distributions on cross-sections of the button model for stationary, centered EB heating with a) no momentum sources, b) only Marangoni force, c) only buoyancy force, d) Marangoni and buoyancy forces, e) Marangoni and Darcy forces, and f) Marangoni, buoyancy, and Darcy forces. Lines representing the liquidus (red) and solidus (blue) isotherms superimposed on contour images

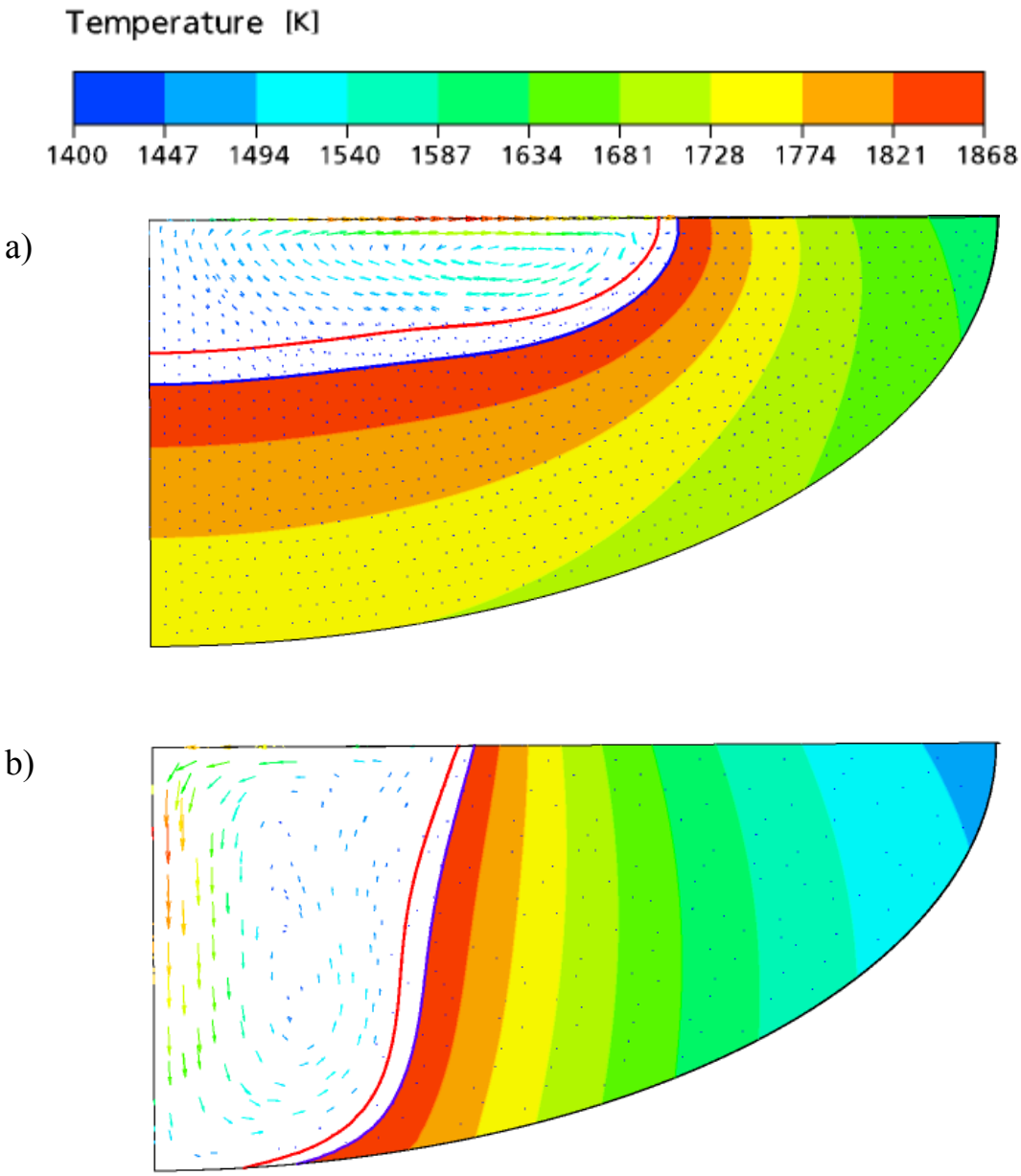

Figure 5.3 Predicted temperature and velocity distributions on cross-sections of the button model (considering only Marangoni forces) for stationary, centered EB heating with a) negative and b) positive surface tension coefficients. Predictions include velocity vectors overlaid on temperature contours (up to the solidus temperature) and line representing the liquidus (red) and solidus (blue) isotherms

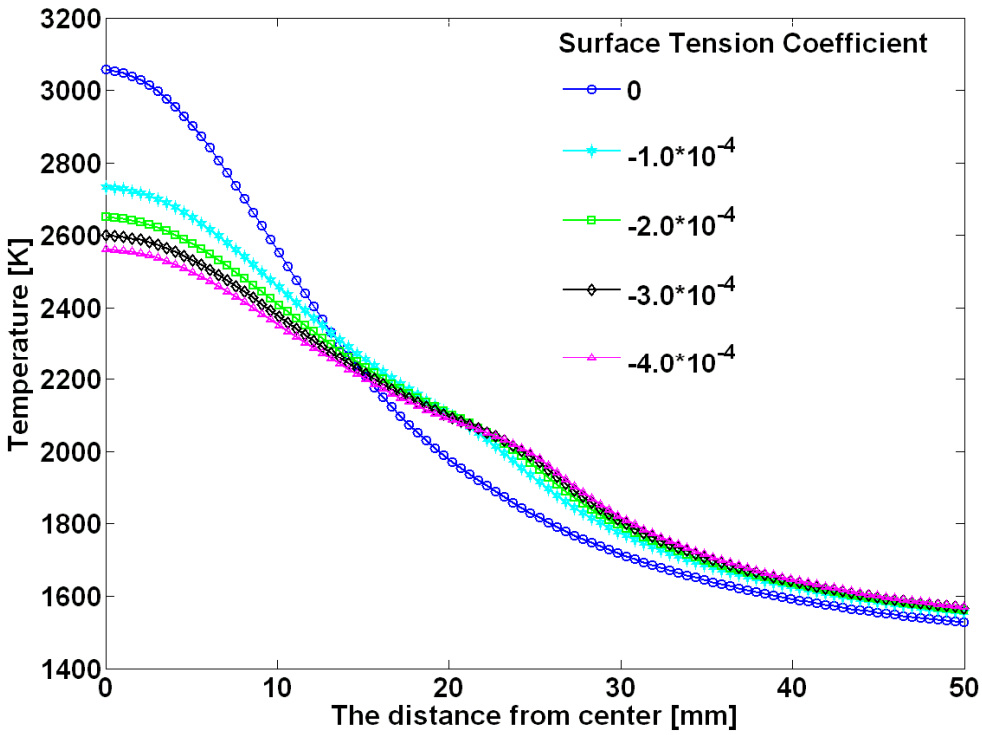

Figure 5.4 Predicted temperature distributions on the top surface of the button for stationary, centered EB heating with varying surface tension coefficients. (only Marangoni forces considered)

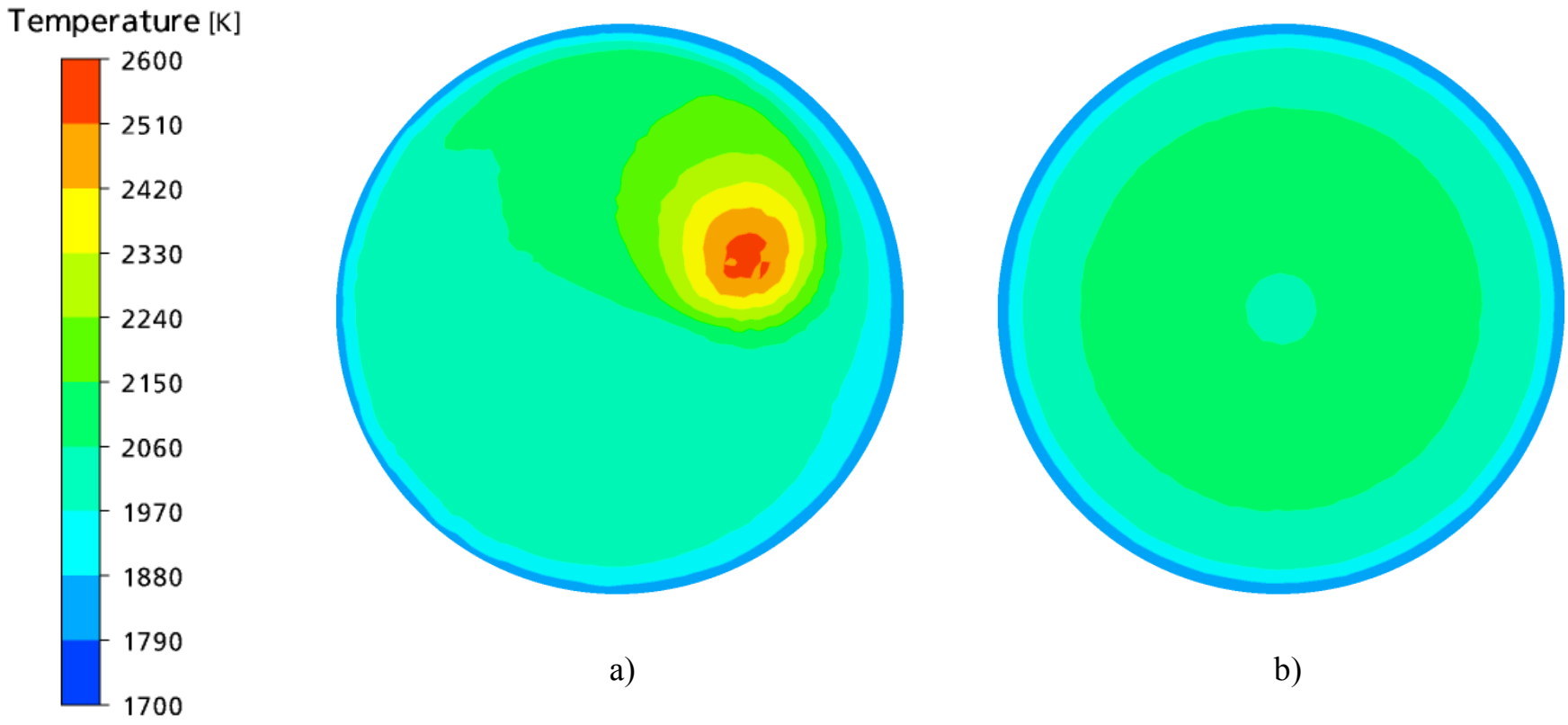

Figure 5.5 Predicted temperature contours on the top surface of the button for the a) moving EB heating and b) time-averaged EB heating conditions. (Cycle time = 1.6s for moving heating condition)

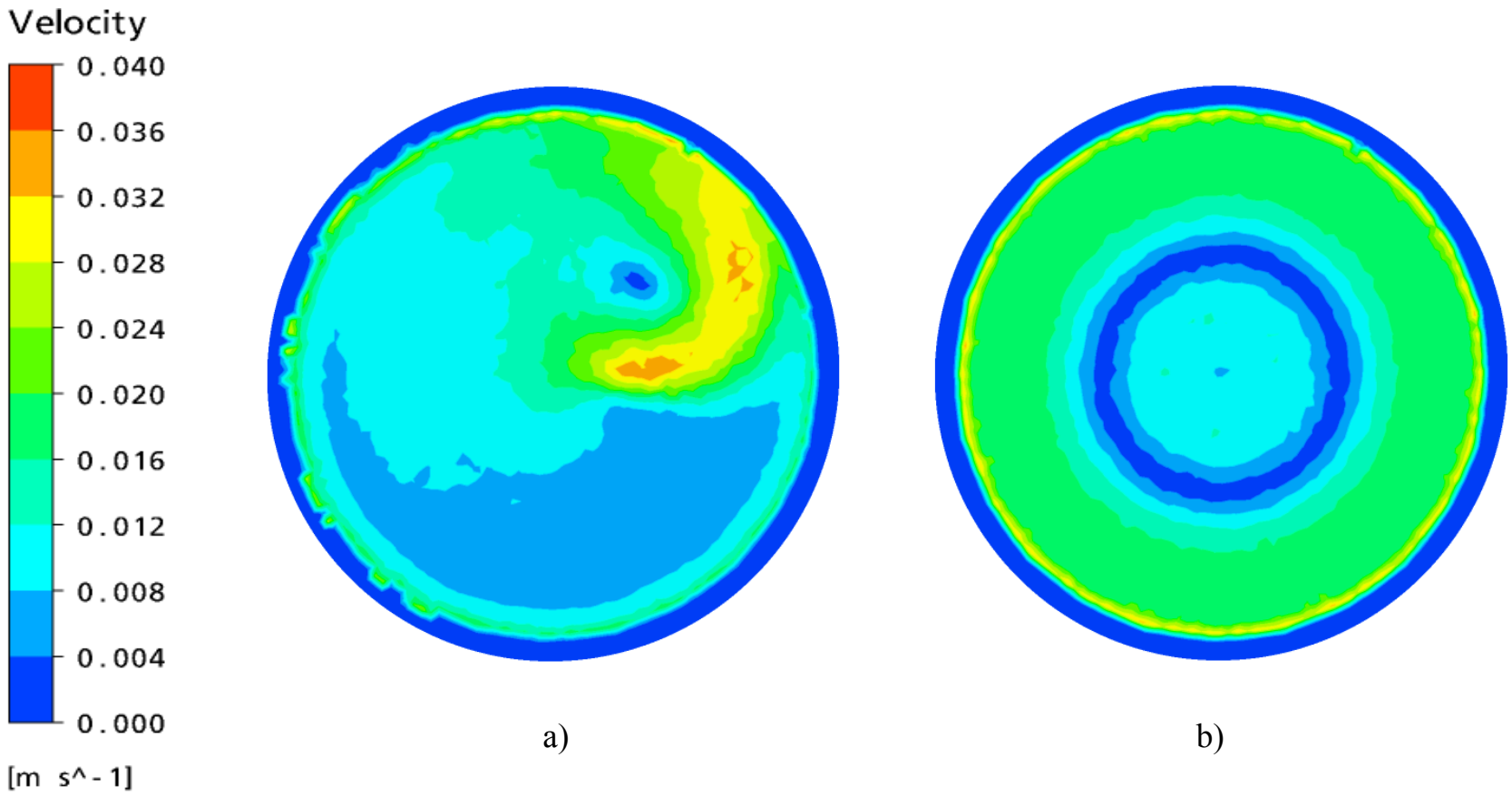

Figure 5.6 Predicted velocity contours on the top surface of the button for the a) moving EB heating and b) time-averaged EB heating conditions. (Cycle time = 1.6s for moving heating condition)

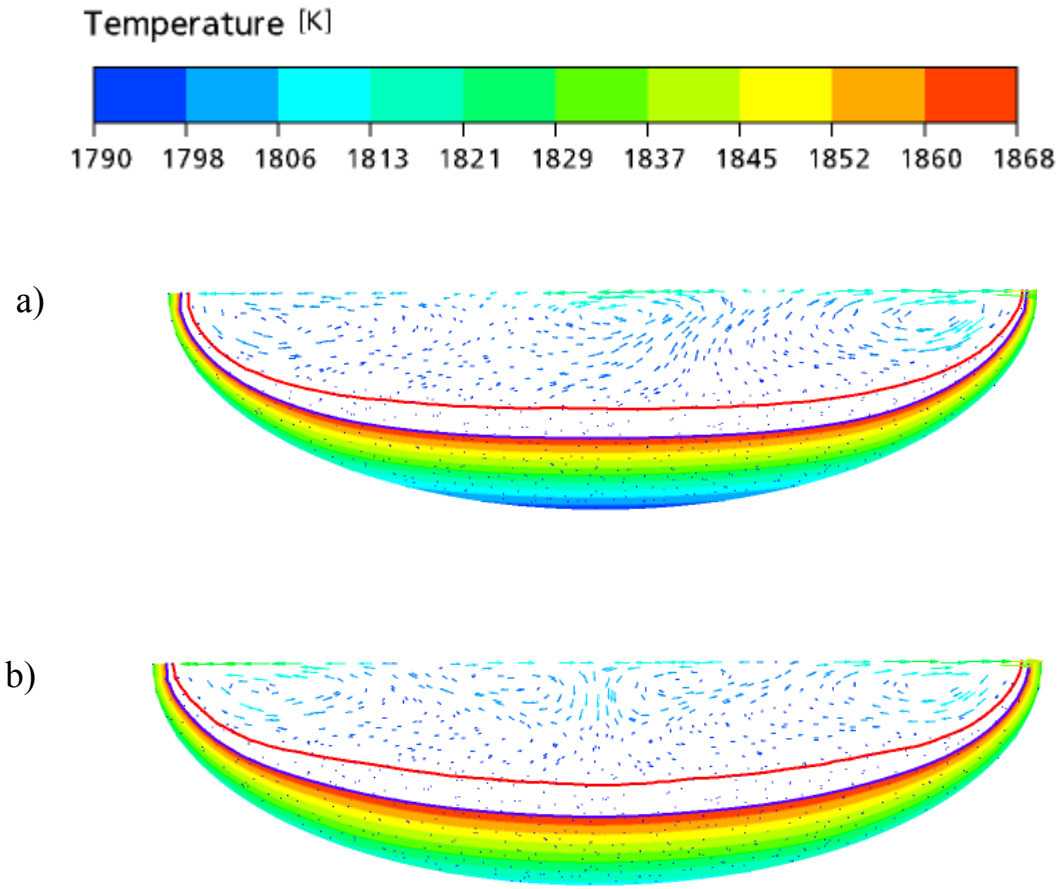

Figure 5.7 Predicted velocity vectors, liquid pool and temperature contours in the solid on across-section of the button for the a) moving EB heating and b) time-averaged EB heating conditions. Lines indicate the liquidus isotherm (red) and solidus isotherm (blue). (Cycle time = 1.6s for moving heating condition)

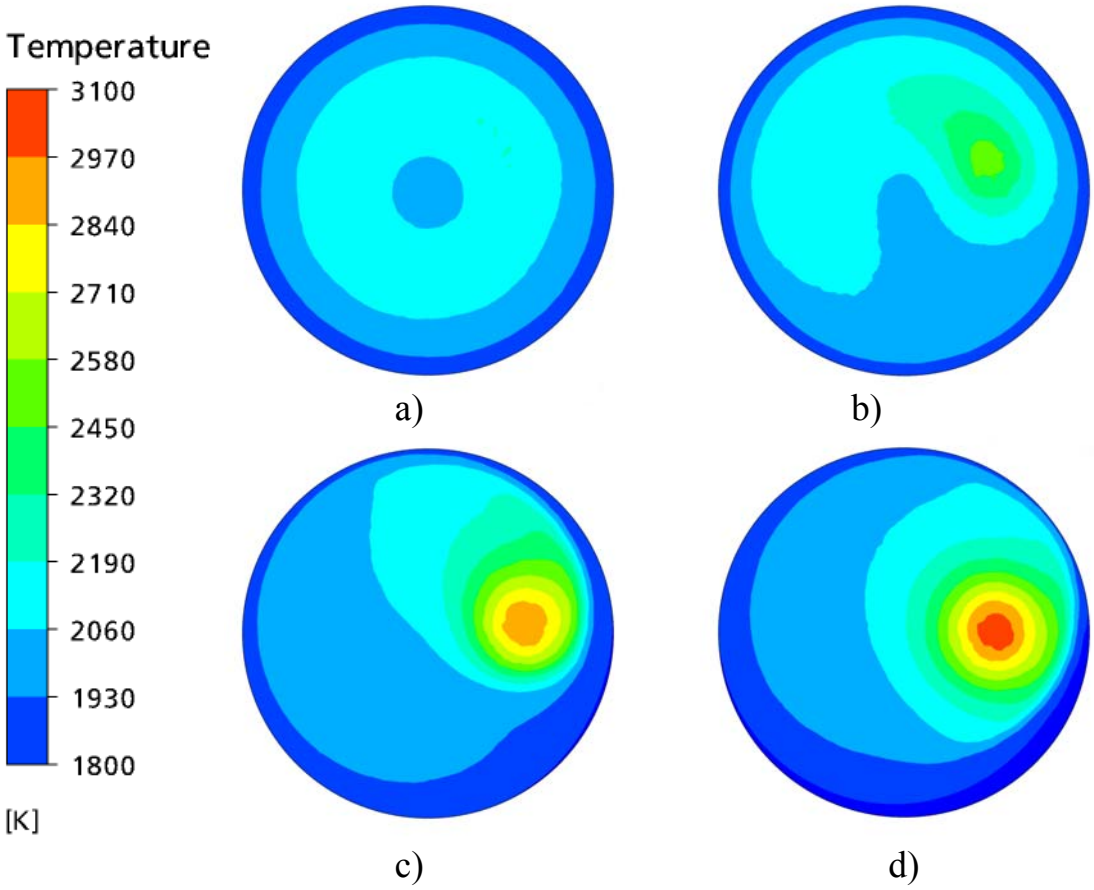

Figure 5.8 Predicted temperature contours on the top surface of the button for the moving EB heating for the cycle time = a) 0.1s, b) 1s, c) 5s and d) 10s

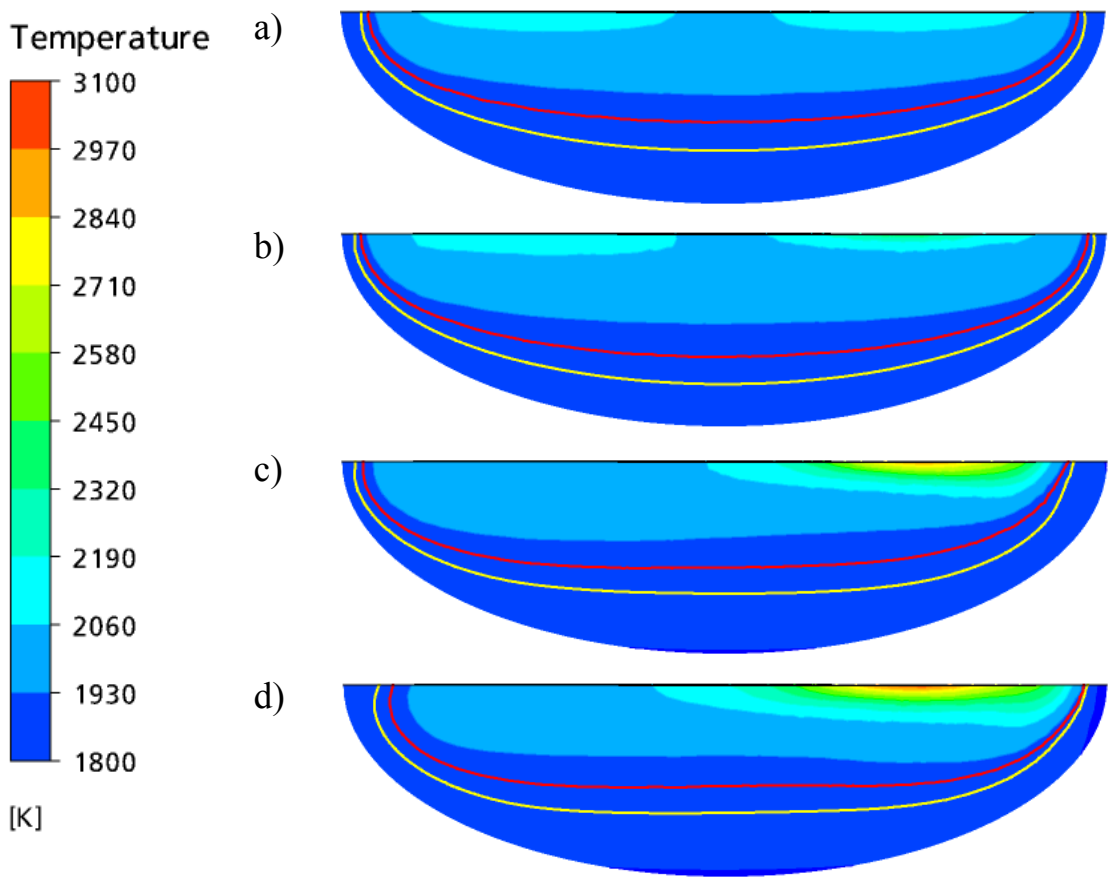

Figure 5.9 Predicted temperature contours on a cross section of the button model for the moving EB heating for the cycle time = a) 0.1s, b) 1s, c) 5s and d) 10s. Lines indicate the liquidus isotherm (red) and the solidus isotherm (yellow)

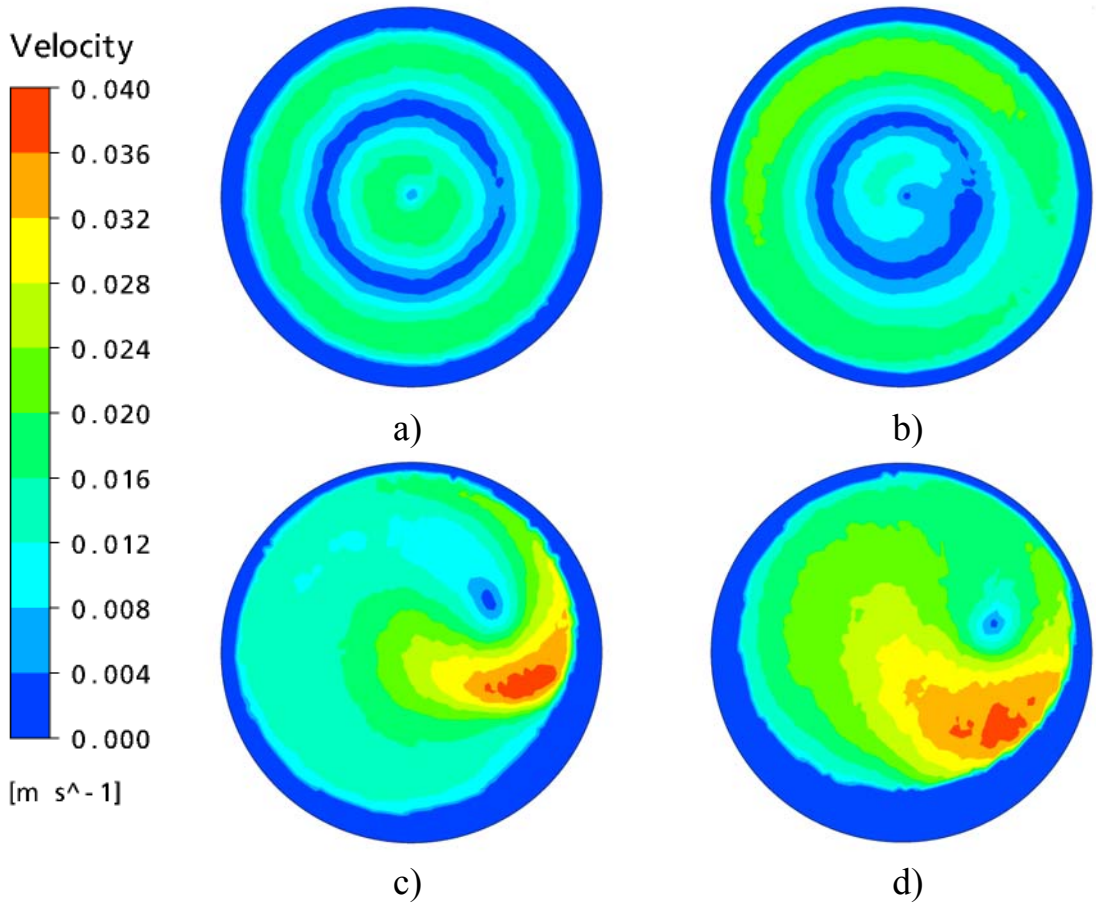

Figure 5.10 Predicted velocity contours on the top surface of the button for the moving EB heating for cycle times of a) 0.1s, b) 1s, c) 5s and d) 10s

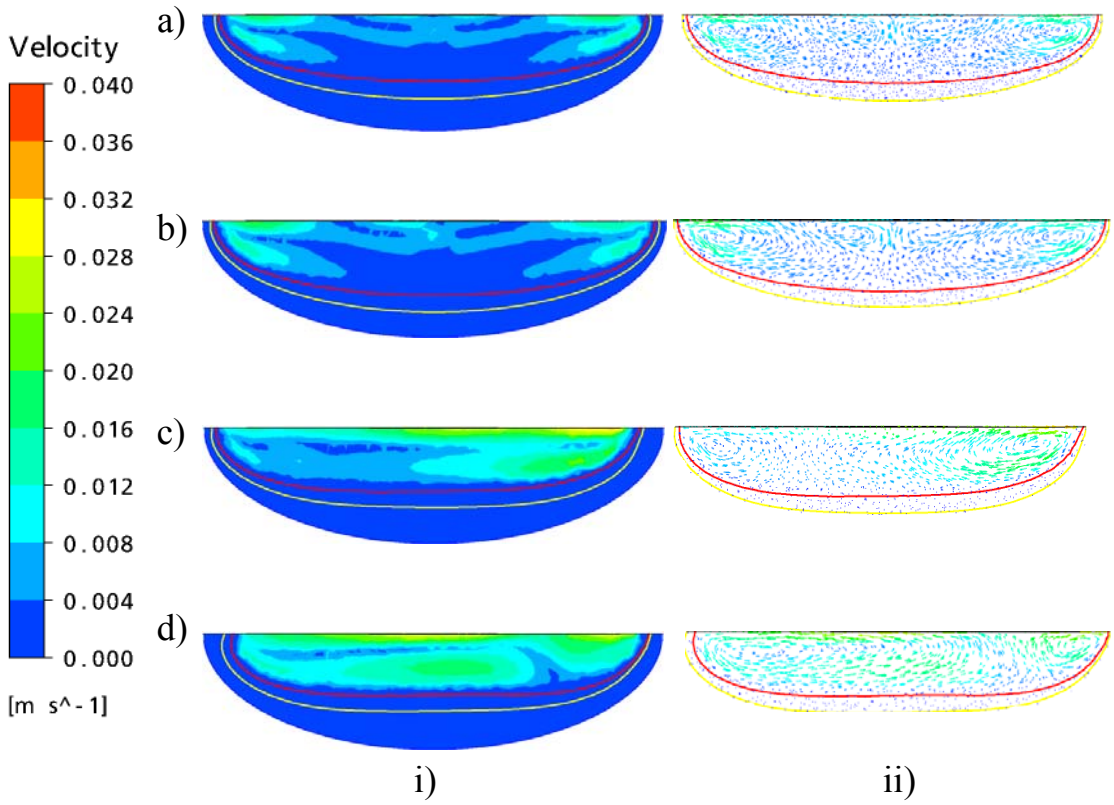

Figure 5.11 Predicted velocity i) contours and ii) vectors on cross sections of the button model for the moving EB heating for the cycle time = a) 0.1s, b) 1s, c) 5s and d) 10s. Lines indicate the liquidus isotherm (red) and solidus isotherm (yellow)

a)

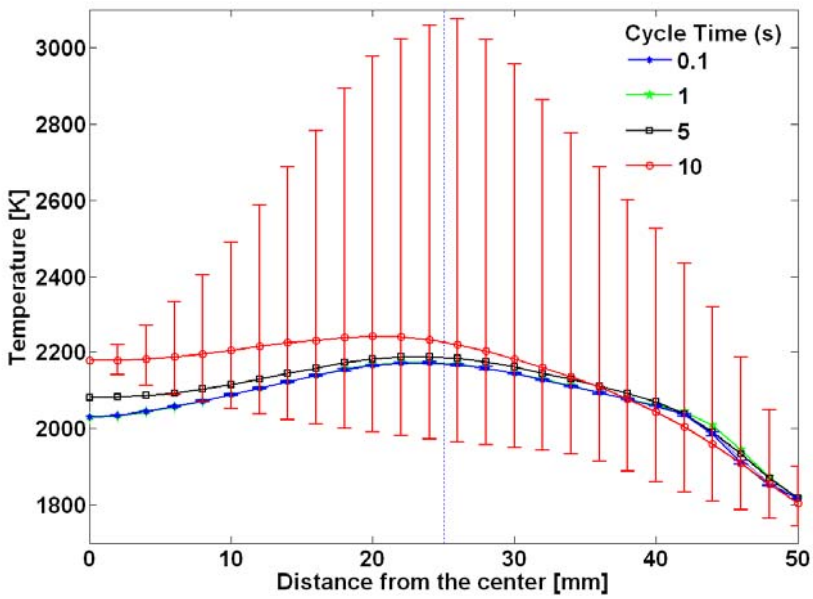

b)

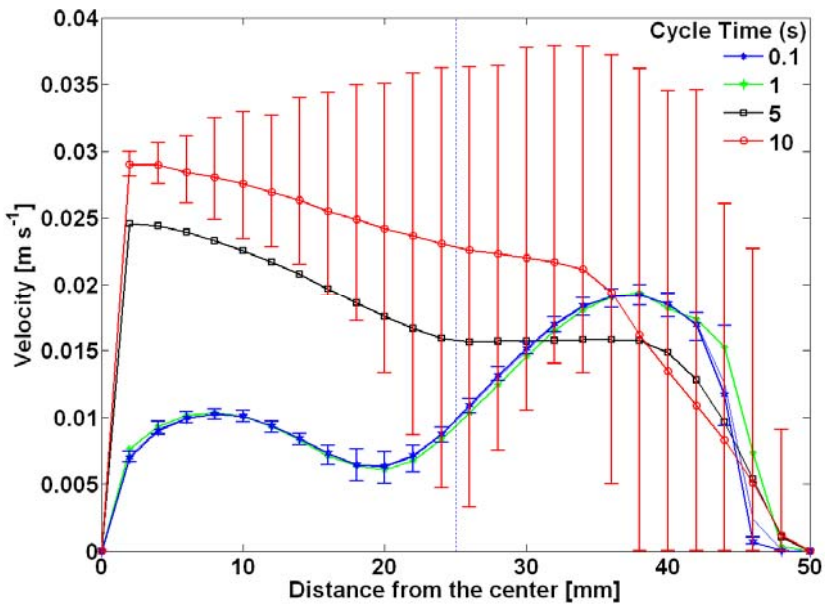

Figure 5.12 Circumferentially averaged a) temperature and b) velocity on the top surface of button at different distances from the center for moving EB heating conditions with cycle times of 0.1, 1, 5, and 10 s. The dashed lines indicate the center of the beam spot

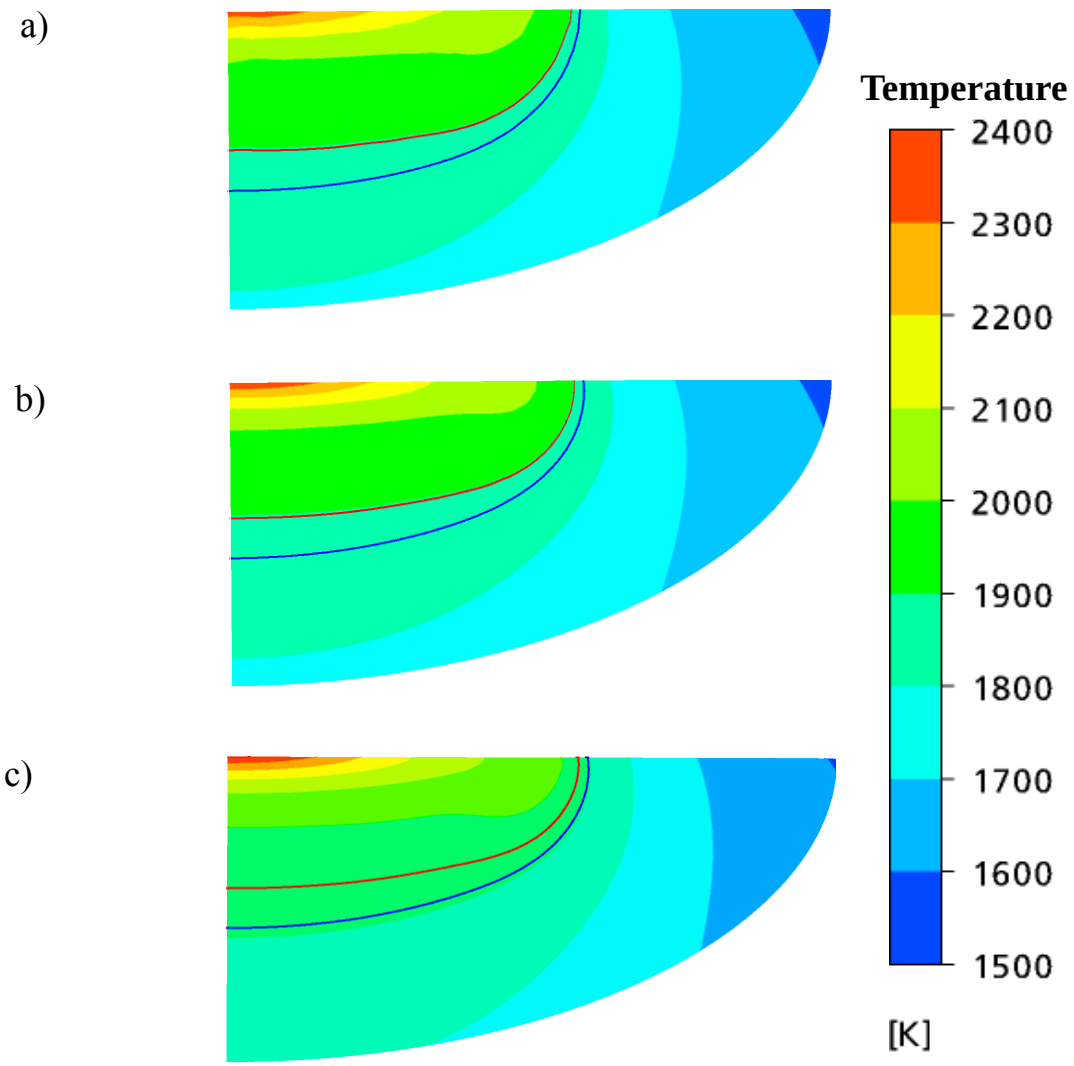

Figure 5.13 Predicted temperature distributions on a cross-section of the button model for sensitivity analysis of a) coarse, b) medium, and c) fine meshes

a)

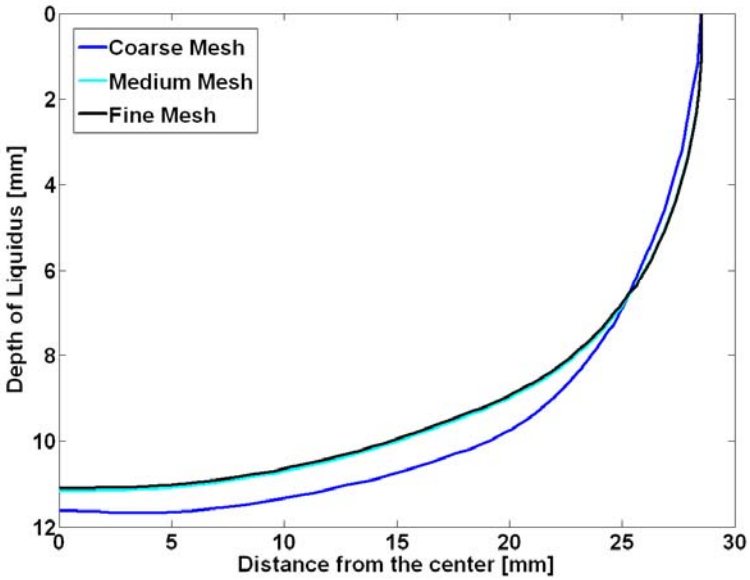

b)

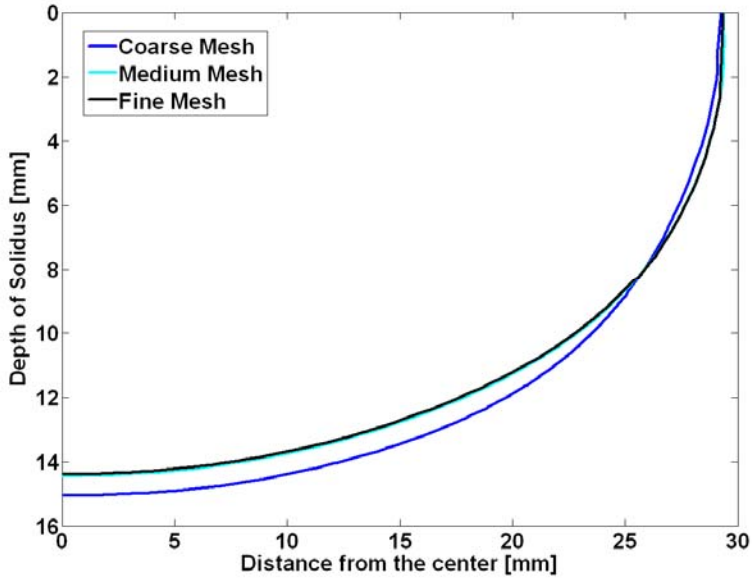

Figure 5.14 Depth of a) liquidus and b) solidus isotherms as a function of distance from the center of the button for coarse, medium, and fine meshes

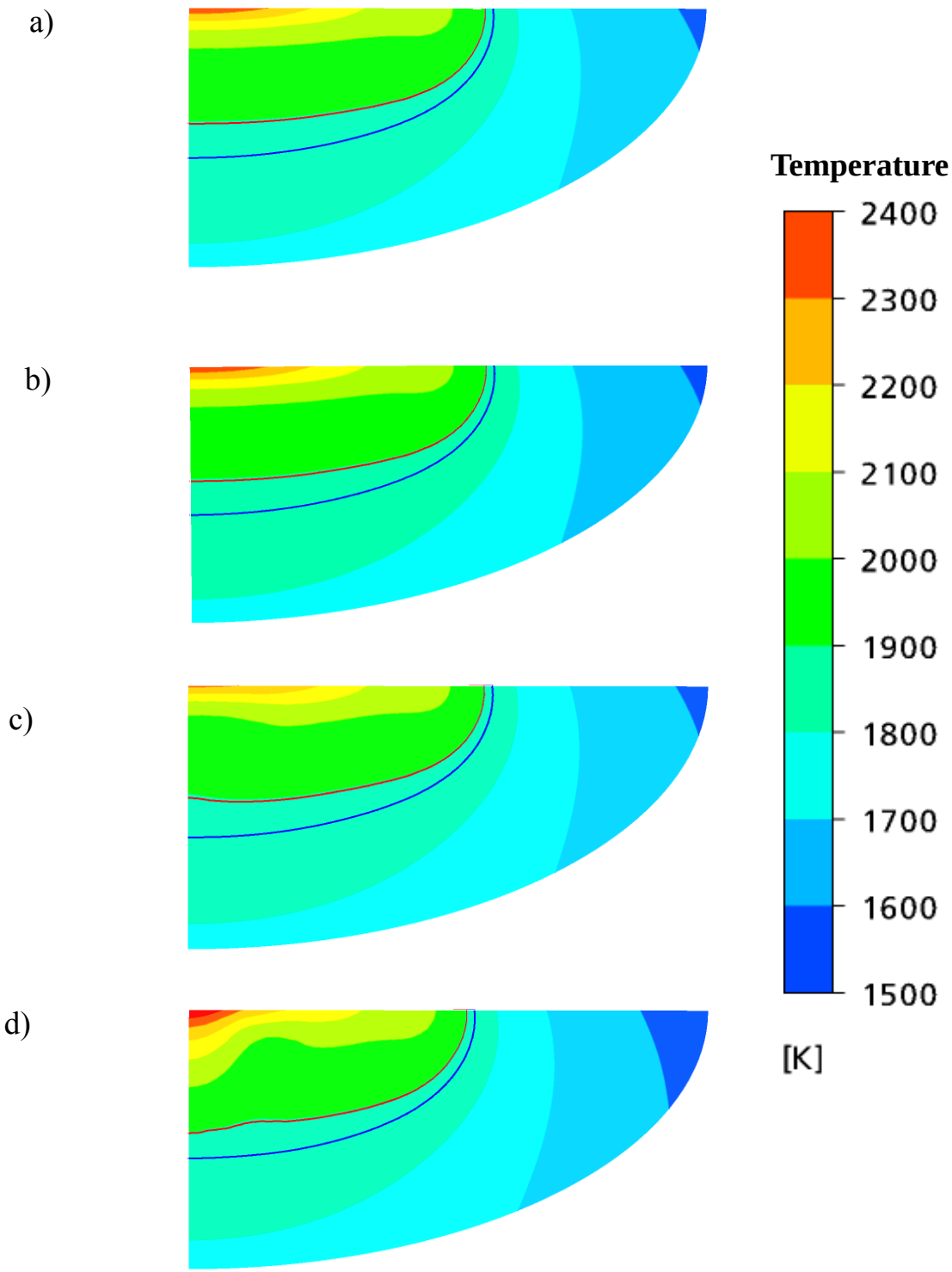

Figure 5.15 Predicted temperature distributions on a cross-section of the button model for sensitivity analysis for time step= a) 0.1s, b) 0.25s, c) 0.5s and d) 1s

a)

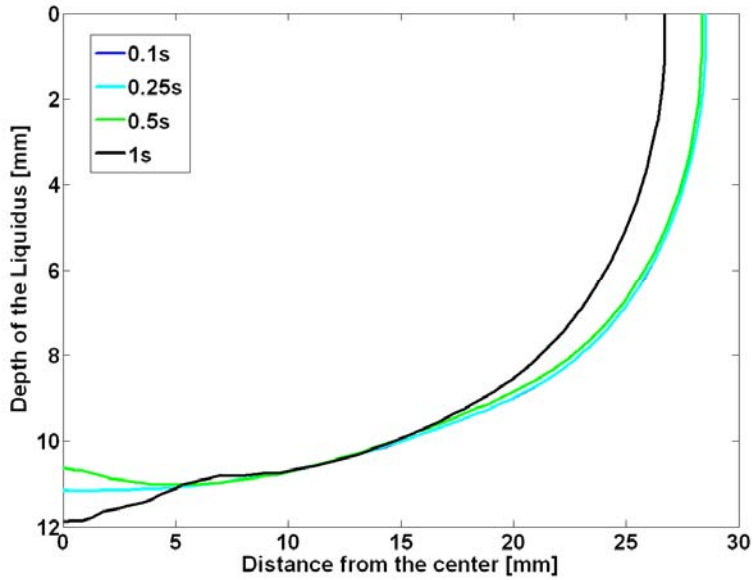

b)

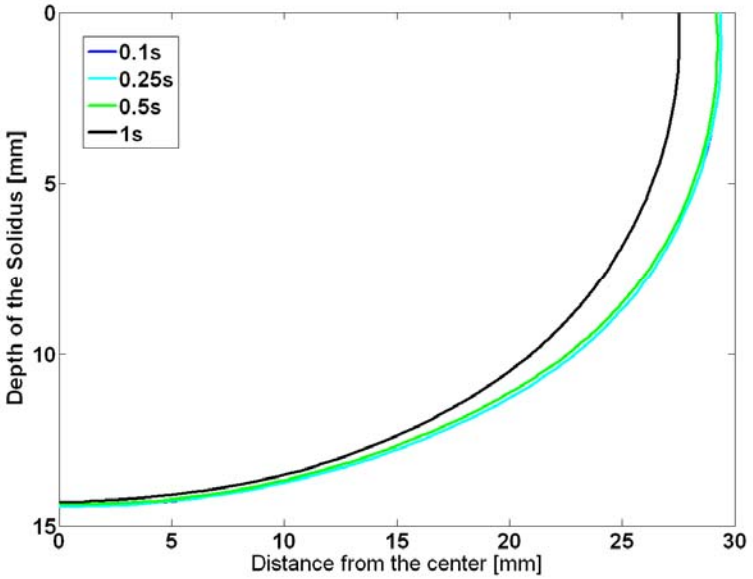

Figure 5.16 Depth of a) liquidus and b) solidus isotherms as a function of distance from the center of the button for time steps of 0.1, 0.25, 0.5, and 1s

a)

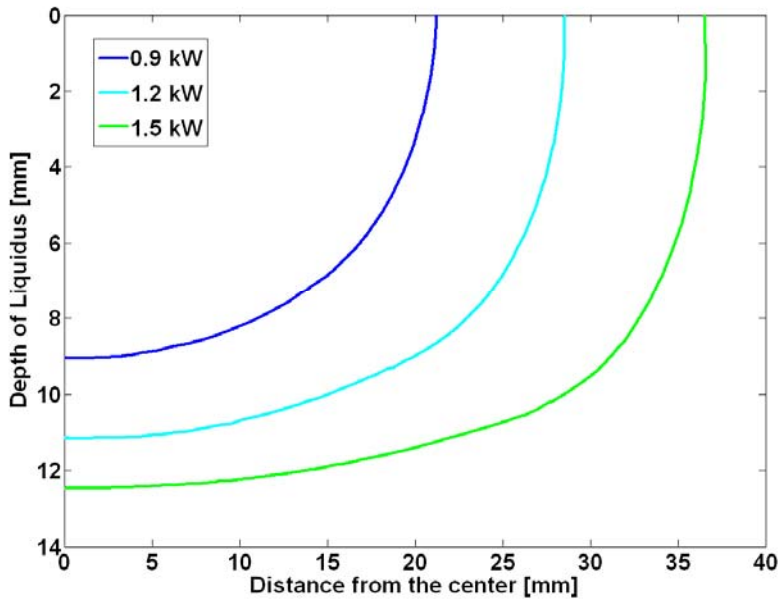

b)

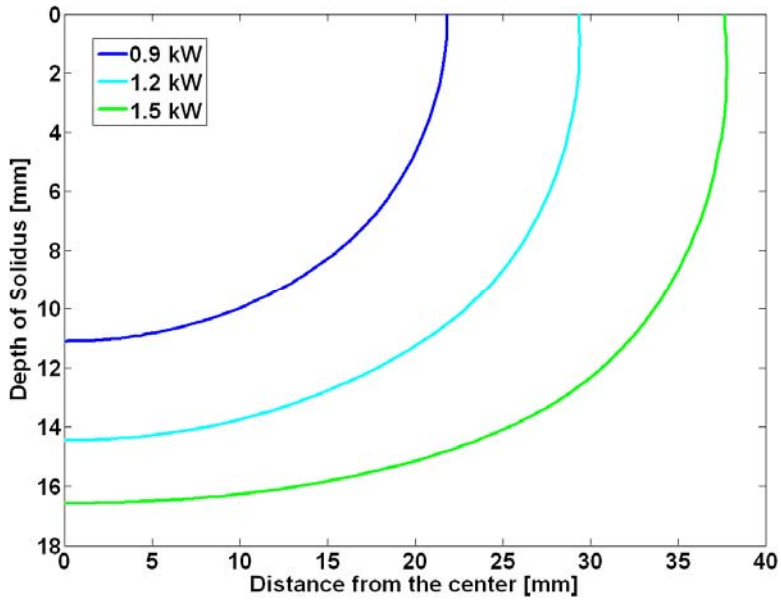

Figure 5.17 Depth of a) liquidus and b) solidus isotherms as a function of distance from the center of the button for electron beam powers of 0.9, 1.2 and 1.5 kW

a)

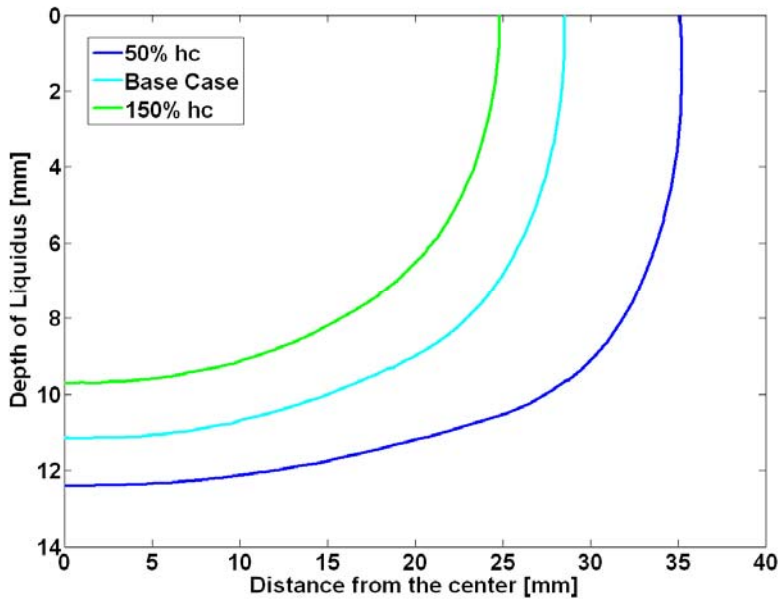

b)

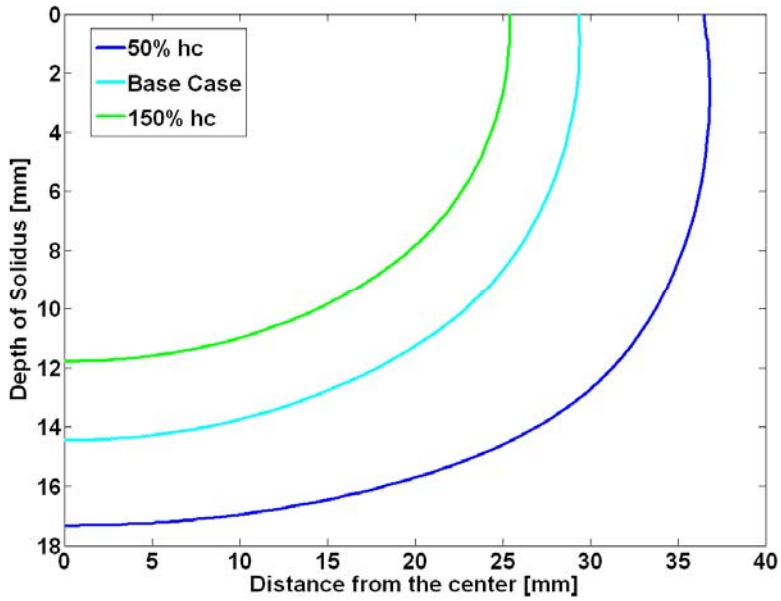

Figure 5.18 Depth of a) liquidus and b) solidus isotherms as a function of distance from the center of the button for heat transfer coefficients (heat loss from the mould) of 50%, 100% (base case) and 150% time the base value

6. Conclusions and Recommendations

6.1 Conclusions

The heat transfer and fluid flow occurring during the electron beam button melting of Ti-6Al-4V has been modeled using the commercial finite volume code Ansys CFX 11.0. The capability of the model to predict the pool shape and top surface temperature distribution were validated through comparison to experimental measurements reported by Richie [23]. The model was then used to assess the relative influences of buoyancy, Marangoni forces and flow damping within the mushy zone on the temperature distributions and flow fields for stationary, centered EB heating conditions.

Marangoni forces cause liquid Ti-6Al-4V to flow from high to low temperature areas resulting in a wider and shallower liquid pool. When the surface tension coefficient was changed to a positive value, flow was directed from low to high temperature areas resulting in a narrower and deeper liquid pool. Additionally, the magnitude of the temperature drop was observed to increase with increasing surface tension coefficient. However, the effect appears to saturate as the surface tension coefficient approaches -4×10^{-4} $kg \cdot s^{-2} \cdot K^{-1}$.

The effect of including buoyancy is similar to that of Marangoni forces, but larger – e.g. for the conditions examined with the model the liquid pool becomes shallower and more spread out with buoyancy alone than with Marangoni alone. The addition of the Marangoni term to buoyancy term resulted in only a small incremental decrease in the pool depth and increase in the pool width. The inclusion of a term in the model to account for mushy zone resistance (Darcy forces) tended to counter the effects of both the Marangoni and buoyancy forces to a significant degree.

It would appear based on the results of the analysis of buoyancy, Marangoni forces and Darcy forces that it is essential to include terms to describe buoyancy driven flow and the attenuation of flow associated with the mushy zone if the object of the model is to predict the liquid pool profile. Inclusion of a term to describe Marangoni forces does not appear to be essential in predicting the liquid pool profile providing the other two momentum sources terms are included. On the other hand, if the objective of the model is to predict evaporation of volatile species accurately, it may be necessary to include Marangoni effects as the associated near surface flow phenomena including the development of recirculation cells in proximity to the beam spot may influence mass transport to the surface and evaporation.

The model was used to assess techniques for describing a moving EB – e.g. treatment of the moving electron beam as a time-averaged heat source vs. as a fully resolved moving heat source. For the time-averaged technique the temperature on the top surface of the button is nearly uniform in a large central region with cooler material on the periphery and in the center. In addition, the temperature distribution on the top surface was found to be radially symmetric. One consequence of the symmetric temperature distribution is that a stable recirculating cell on the scale of the liquid pool is able to develop.

For short beam dwell times (beam cycle time of 0.1 s), the fully resolved approach resulted in nearly identical temperature distributions and flow distributions predicted for the time-averaged case, including the development of symmetric recirculation cells. Increasing the beam pattern cycle time from 1 to 5 s resulted in a significant change to the top temperature distribution including the development of a high temperature region in close proximity to the beam spot. Moreover, longer beam cycle times also resulted in the

development of enhanced fluid flow in the vicinity of the beam spot including the formation of a small-scale recirculating cell in proximity to the beam location. The size of the recirculating cell was found to increase with increasing dwell time due, it is believed, to a combination of the higher temperature gradients, and associated Marangoni forces, and a longer time for the recirculating cell to develop.

Despite the differences described above, the liquid pool shape and mushy zone size for the moving EB and time-averaged EB heating cases were very similar under the conditions examined in this study. It was found that the differences between the two cases, as assessed using circumferentially averaged temperature and velocity values, tended to decrease with the decreasing pattern cycle time (increasing beam pattern repetition frequency). The mean temperature and velocity were nearly identical for the two cases when the beam frequency reached 10 Hz (only about 0.5% difference). The results suggest that if the objective is to model the liquid pool profile a time averaged approach to modeling the heat input is satisfactory over the range of beam pattern frequencies examined with the model. If on the other hand, the objective is to model evaporation accurately it may be necessary to fully resolve the moving beam computationally in order to predict the resulting surface temperature and surface fluid flow transients accurately particularly for high beam pattern cycle times.

A sensitivity analysis was conducted with the model for various numerical, process and model related parameters. Analysis of the numerical parameters indicated that a maximum element edge length of 2 mm and a time step of 0.25 s were appropriate for the current model. The model was shown to be very sensitive to changes in power input and heat transfer coefficient.

6.2 Recommendations for Future Work

Firstly, the model should be modified to include chemical species tracking and evaporation in order that the effect of including surface tension driven flow on evaporation can be investigated. The work should be accompanied by an experimental campaign aimed at producing data suitable for validating the model.

Secondly, using the enhanced version of the model, the effect of the different approaches to modeling the moving EB heat source should be reexamined to see if there is an effect on evaporation and under what conditions it is necessary to fully resolve the moving EB.

References

[1] Periodic Table of the Elements: Los Alamos National Laboratory's Chemistry Division, 2004, pp. 158-159.

[2] J. Barksdale, The Encyclopedia of the Chemical Elements, New York: Reinhold Book Corporation, 1998, pp. 732–738.

[3] "Titanium", Columbia Encyclopedia (6th edition ed.), New York: Columbia University Press, 2006.

[4] N. Casillas, S. Charlebois, W. H. Smyrl, and H. S. White, "Pitting corrosion of titanium," J. Electrochem. Soc., vol. 141, pp. 636 – 642, 1994.

[5] J. Emsley, Nature's Building Blocks: An A-Z Guide to the Elements Oxford, England, UK: Oxford University Press, 2004, p. 452.

[6] J. Matthew and J. Donachie, TITANIUM: A Technical Guide, Metals Park, OH: ASM International, 1988.

[7] G. Z. Chen, D. J. Fray, and T. W. Farthing, "Direct electrochemical reduction of titanium dioxide to titanium in molten calcium chloride," Nature, vol. 407, pp. 361 –64, 2000.

[8] P. Yuan, S. Shesh, and O. Y. Kuang, "Electron Beam melting and plasma arc melting," modeling for casting and solidification processing, Materials Engineering, vol. 19, pp. 613-653, 2002.

[9] Vacuum Arc Remelting (VAR), Hanau, Germany: ALD Vacuum Technologies.http://web.ald-vt.de/cms/vakuum-technologie/anlagen/vacuum-arc-remelting-var/, 2000.

[10] Y. Ko, "Plasma arc melting for titanium alloys," in Proceedings of the Technical Program from the 1998 International Conference, Monte Carlo, Monaco, 1998, pp. 371-385.

[11] Y. Ko, "PAM processing titanium alloys," in Proceeding of Manufacturing technology for aerospace materials: A Technology Demonstration and Information Exchange, Arlington, VA, 1999, pp. 58-74.

[12] S. Schiler, U. Heisig, and S. Panzer, Electron beam technology, New York: John Wiley & Sons, 1982, p. 508.

[13] X. Zhao, "Mathematical modeling of electron beam cold hearth casting of titanium

alloy ingots," Master's Thesis, The University of British Columbia, 2006.

[14] D. Ablitzer, "Transport phenomena and modeling in melting and refining processes," Journal De Physique IV, vol. 3, pp. 873-882, 1993.

[15] P. Sahoo, T. Debroy, and M. J. Mcnallan, "Surface tension of binary metal – surface active solute systems under conditions relevant to welding metallurgy," Metallurgical Transitions B-Process Metallurgy, vol. 19, pp. 483-491, 1988.

[16] K. Lin, P. Dold, and K. W. Benz, "Numerical study of influences of buoyancy and solutal Marangoni convection on flow structures in a germanium-silicon floating zone," Crystal Research and Technology, vol. 40, pp. 550-556, 2005.

[17] P. S. Nita, "Values of the solutal Marangoni number in very dilute Fe-C-O solutions at 1873K," The Annals of " Dunarea De Jos": University of Galati, pp. 142-144, 2007.

[18] K. Vutova and G. Mladenov, "Computer simulation of the heat transfer during electron beam melting and refining," Vacuum, vol. 53, pp. 87-91, 1999.

[19] H. Nakamura and A. Mitchell, "The effect of beam oscillation rate on Al evaporation from a Ti-6Al-4V alloy in the electron beam melting process," ISIJ International, vol. 23, pp. 583-592, 1992.

[20] H. Hao, D. M. Maijer, M.A. Wells, S.L. Cockroft, D. Sediako, and S. Hibbins, "Development and validation of a thermal model of direct chill casting of AZ31 magnesium Bbillets", Metallurgical and Materials Transactions A, vol. 35A, pp. 3843-3854, 2004.

[21] J. P. Bellot and D. Ablitzer, "Balance of particle removal against aluminum losses in EBCH melting of Ti alloys," in EBEAM 2002 International Conference on High-Power Electron Beam Technology, Crowned Plaza Resort, Hilton Head Island, South Carolina, pp. 1-4, 2002.

[22] M. K. Kelkar, V. P. Suhas, and K. S. Shesh, "Mathematical modeling of the electron beam cold hearth refining of titanium alloys," in Proceeding of the Conference on Electron Beam Melting and Refining – State of the Art, Reno, NV, 1997, pp. 238-251.

[23] M. T. Ritchie, "EDX investigation of evaporative losses during the EB melting of SS316," PhD's Thesis, The University of British Columbia, 1997.

[24] Malcolm D. Lane, "A coupled thermal – fluid flow model of the horizontal direct chill casting process for T-Ingot", Master's Thesis, The University of British

Columbia, 2006.

[25] W. Shyy, Y. Pang, G. B. Hunter, D. Y. Wei, and M. H. Chen, "Effect of turbulent heat transfer on continuous ingot solidification," Journal of Engineering Materials and Technology, vol. 115, pp. 8-16, 1993.

[26] S. Chakraborty, N. Chakraborty, P. Kumar and P. Dutta, " Studies on turbulent momentum, heat, and species transport during binary alloy solidification in a top-cooled rectangular cavity", International Journal of Heat and Mass Transfer, vol. 46, pp. 1115-1137, 2003.

[27] K. Han, "Numerical investigation on the heat transfer characteristics of a liquid-metal pool subjected to a partial solidification process" Progress in Nuclear Energy, vol. 44, pp. 277-304, 2004.

[28] H. Wei, Y.S. Chen and H.M. Shang, "The study of flow pattern and phase-change problems in die casting process", American Institute of Aeronautics and Astronautics, pp. 1806, 1996.

[29] T. Isawa, H. Nakamura, and K. Murakami, "Aluminum evaporation from titanium alloys in EB hearth melting process," ISIJ International, vol. 32, pp. 607-615, 1992.

[30] I. Langmuir, Physics Review, pp. 329-342, 1913.

[31] A. Powell, J. V. Avyle, and B. Damkroger, "Analysis of multicomponent evaporation in electron beam melting and refining of titanium alloys," Metallurgical and Materials Transactions B, vol. 28, pp. 1227-1239, 1997.

[32] S. Cockcroft, A. Mitchell, and D. Tripp, "Evaporation in the EBCHM process," in Proceedings of Conference on Electron Beam Melting and Refining – State of Art, Reno, NV, USA, 1992.

[33] S. Fukumoto, "Composition control of refractory and reactive metals in electron beam melting," ISIJ International, vol. 32, pp. 664-672, 1992.

[34] M. Ritchie and A. Mitchell, in Proceedings of the Conference on Electron Beam Melting and Refining – State of Art, Reno, NV, USA, 1996.

[35] S. V. Akhonin, N. P. Trigub, V. N. Zamkov, and S. L. Semiatin, "Mathematical modeling of aluminum evaporation during electron-beam cold-hearth melting of Ti-6Al-4V ingots, "Metallurgical and Materials Transactions B, vol. 34, pp. 447-454, 2002.

[36] P. D. Lee, P. N. Quested, and M. Mclean, "Modelling of Marangoni effects in

electron beam melting," Philosophical Transactions of the Royal Society A-Mathematical Physical and Engineering Sciences, vol. 356, pp. 1027-1043, 1998.

[37] K. C. Mills, Recommended values of thermophysical properties for selected commercial alloys, Materials Park: Woodhead Publishing Ltd and ASM International, 2002.

[38] User Guide for Ansys CFX 11.0, 2006.

[39] L. Xueping, P. Xiaofeng, and W. Buxuan, "Influence of Marangoni flow on the melting process," Progress in Natural Science, vol. 7, pp. 616-623, 1997.

[40] Y. Z. Zhao, H. Y. Zhao, and Y. P. Lei, "Theoretical study of Marangoni convection and weld penetration under influence of high oxygen content in base metal," Science and Technology of Welding and Joining, vol. 12, pp. 410-417, 2007.

[41] L. X. Yang and X. F. Peng, "Numerically modeling and characteristics of molten pool during laser processing," Journal of Basic Science and Engineering, vol. 9, pp. 215-221, 2001.

[42] M. R. Amin and A. Mahajan, “Modeling of turbulent heat transfer during the solidification process of continuous castings,” Journal of Materials Processing Technology, vol. 174, pp. 155-166, 2006.

[43] M. C. Flemings, Solidification Processing, New York: McGraw-Hill, 1974.

[44] M. Rappaz, “Modelling of microstructure formation in solidification process,” International Materials Review, vol. 34, pp. 93-123, 1989.

[45] X. Zhao, D.M. Maijer, S.L. Cockcroft, D. Tripp, S. Fox, and J. Zhu, “A three-dimensional steady state thermal fluid model of ingot casting process associated with electron beam melting of Ti -6Al-4V,” in the 11th World Conference on Titanium, Kyoto, Japan, June 2 – 7, 2007.

[46] E. A. Brandes, C. J. Smithells, Smithells Metals Reference Book, Oxford: Butterworth-Heinemann, 7th Edition, 1999.

[47] R. Aune, R. Wunderlich, and L. Battezati, “Surface tension and viscosity of industrial alloys from parabolic flight experiments – results of the thermolab experiments,” Microgravity Science and Technology, vol. 16, pp.11-14, 2005.